A probabilistic approach to seismic diffraction imaging[a]

[a]Published in Lithosphere, v. 2021, no. 1, 6650633 (2021)

Luke Decker and Sergey Fomel

ABSTRACT

We propose and demonstrate a probabilistic method for imaging seismic diffractions based on path-integral imaging. Our approach utilizes oriented velocity continuation to produce a set of slope-decomposed diffraction images over a range of plausible migration velocities. Utilizing the assumption that each partial image in slope is independent enables us to construct an object resembling a probability field from the slope-decomposed images. That field may be used to create weights for each partial image in velocity corresponding to the likelihood of a correctly migrated diffraction occurring at a location within the seismic image for that migration velocity. Stacking these weighted partial images over velocity provides us with a path-integral seismic diffraction image created using probability weights. We illustrate the principles of the method on a simple toy model, show its robustness to noise on a synthetic, and apply it to a 2D field dataset from the Nankai Trough. We find that using the proposed approach creates diffraction images that enhance diffraction signal while suppressing noise, migration artifacts, remnant reflections, and other portions of the wavefield not corresponding to seismic diffraction relative to previously developed diffraction imaging methods, while simultaneously outputting the most likely migration velocity. The method is intended to be used on data which has already had much of the reflection energy removed using a method like plane-wave destruction. Although it suppresses residual reflection energy successfully, this suppression is less effective in the presence of strong reflections typically encountered in complete field data. The approach outlined in this paper is complimentary to existing data domain methods for diffraction extraction, and the probabilistic diffraction images it generates can supplement existing reflection and diffraction imaging methods by highlighting features that have a high likelihood of being diffractions and accentuating the geologically interesting objects in the subsurface that cause those features.

INTRODUCTION

Though less popular than reflection imaging for characterizing the subsurface, diffraction imaging has been gaining increasing attention (Landa, 2012). Seismic diffractions

occur when a seismic wave interacts with an object on the order of its wavelength, such as a fault, fracture, or void (Harlan et al., 1984; Fomel et al., 2007; Moser and Howard, 2008; Klokov and Fomel, 2012; Decker et al., 2015; Popovici et al., 2015; Schwarz, 2019), and may even be able to resolve objects beyond the seismic wavelength (Khaidukov et al., 2004).

Seismic diffractions are significantly weaker than reflections (Klem-Musatov, 1994), requiring their quarantining from the stronger reflection signal to be usable. Numerous methods exist for separating diffraction signal from reflection, in both the data and image domains (Harlan et al., 1984; Kozlov et al., 2004; Fomel et al., 2007; Moser and Howard, 2008; Berkovitch et al., 2009). Attributes correlated to a diffraction occurring, like focusing (Khaidukov et al., 2004) or angle-gather flatness (Landa et al., 2008; Reshef and Landa, 2009) only become available after migration, so these methods typically function by predicting and removing reflections, although recent excitement in applying machine learning techniques to problems related to seismic imaging and interpretation (Pham et al., 2019; Kaur et al., 2019; Wu et al., 2020) has extended into the use of pattern recognition (de Figueiredo et al., 2013 and deep learning (Tschannen et al., 2020) for diffraction detection. Reflection removal leaves the diffractions but also the already present noise. Diffraction images often feature poor signal to noise ratios and situations where it is difficult to distinguish what features are diffraction, noise, or migration artifacts (Harlan et al., 1984; Fomel et al., 2007; Decker et al., 2013). This difficulty motivated Decker et al. (2017b) to treat the semblance of diffraction image angle gathers as a proxy for diffraction likelihood at different locations in space, and use that semblance as a model weight for least-squares Kirchhoff migration (Nemeth et al., 1999). However, in practice this involved thresholding semblance at a selected level, making the process both arbitrary and non-linear. To overcome this issue we turn to path-integral seismic imaging.

Path-integral seismic imaging (Landa et al., 2006) applies the stationarity of Feynman path integrals to the problem of seismic time imaging to create images without knowing a velocity model. Integrating (stacking) over all possible seismic signal paths, which are dependent on velocity, with an appropriate weighting function produces a seismic image based on the concept that the seismic image is stationary at the correct velocity. Thus, paths with incorrect velocity interfere destructively during summation whereas correct velocity signal interferes constructively. Schleicher and Costa (2009) utilized this concept to determine seismic migration velocity, while Burnett et al. (2011), Merzlikin and Fomel (2017), Merzlikin et al. (2019), and Merzlikin et al. (2020) applied the technique to seismic diffraction imaging.

We observe that if the weight functions used in the path-integral imaging equations are treated as probability distributions, the imaging and velocity analysis techniques become equivalent to calculating expectation values for the time image and time migration velocity respectively (Fomel and Landa, 2014). This is immediately clear when examining the imaging condition of Landa et al. (2006), which treats the imaging process as a weighted summation of images within a set corresponding to the probability of each. This observation inspires us to use attributes corresponding to

diffraction probability as weight functions. In order to utilize such a framework we first need a suite of seismic images over different migration velocities and their angle gathers, which are provided by oriented velocity continuation (OVC). OVC involves the continuous propagation of slope-decomposed seismic images along their characteristics over different time migration velocities (Decker and Fomel, 2014; Decker et al., 2017a). Other continuation operators exist, for example Burnett and Fomel (2011) proposed a method for applying azimuthally anisotropic velocity continuation to zero-offset data. The slope-decomposed partial images produced by OVC are equivalent to dip-angle gathers (Decker and Klokov, 2014), enabling us to compute gather semblance and other path-integration weights. OVC provides us with an ensemble of slope-decomposed seismic images over a range of different time migration velocities. We propose to use these images to construct the weight functions for path integration.

This paper demonstrates the principles of our probabilistic imaging process and applications to demonstrate its utility. In the next section we outline how we may construct weight functions for path-integral imaging correlated to the probability of a correctly migrated diffraction occurring at a location in space for a given velocity. We illustrate our methodology on a toy model example and then apply it to a synthetic data set to illustrate its robustness to noise relative to deterministic methods for diffraction imaging and equal weight path-integral imaging. The method is applied to a field data set of the Nankai trough to show how it is able to both generate a diffraction image with suppressed noise and output a plausible velocity field that is able to highlight geologically interesting features like a velocity inversion. Finally, we end the paper with conclusions and outline some promising avenues for future work.

THEORY

We may write the imaging condition of Landa et al. (2006) for weighted path-integral image Q_w, weights $w(\eta)$, stack $Q(\eta)$ and wavefront multiparameter η, which parameterizes all possible ray paths as:

$$Q_w = \int w(\eta)\ Q(\eta)\ d\eta. \tag{1}$$

Allowing $w(\eta)$ to be a probability distribution, Q_w becomes an image expectation value. For the case of time migration, ray paths are uniquely parameterized by velocity, so η in the above equation may be replaced by v. A deterministic image would use a Dirac delta at the most likely velocity as the weight function. To create our weight functions we will apply Oriented Velocity Continuation (OVC) to generate a collection of slope-decomposed seismic images over different migration velocities, $I(\mathbf{x}, v, p)$, where $\mathbf{x}$ is a vector describing the position within a seismic image, v is the migration velocity, and p is the image slope. If we consider each slope-decomposed seismic trace within a gather at position $\tilde{\mathbf{x}}$ at velocity $\tilde{v}$, $I(\tilde{\mathbf{x}}, \tilde{v}, p)$, to be independent, we may calculate gather semblance and treat it as a likelihood of a properly migrated seismic diffraction event occurring at that location. This is based on the observation

that diffractions migrated with correct velocity possess flat angle-gathers. The semblance, $\alpha \in [0,1]$, which will serve as our first weight for path integration, may be calculated as:

$$\alpha(\mathbf{x},v) = \frac{\left(\int I(\mathbf{x},v,p)\,dp\right)^2}{\int I(\mathbf{x},v,p)^2\,dp}, \tag{2}$$

$$W_1(\mathbf{x},v) = \alpha(\mathbf{x},v). \tag{3}$$

Note that unbounded integrals are considered to be over the whole domain of the integrating variable. To avoid issues related to dividing by 0, all division operations are treated as an inversion involving shaping regularization (Fomel, 2007). Semblance may be used additionally to calculate the expectation velocity $\bar{v}(\mathbf{x})$ at each location $\mathbf{x}$ and the corresponding velocity variance, $\sigma_v^2(\mathbf{x})$:

$$\bar{v}(\mathbf{x}) = \frac{\int v\,\alpha(\mathbf{x},v)\,dv}{\int \alpha(\mathbf{x},v)\,dv}, \tag{4}$$

$$\sigma_v^2(\mathbf{x}) = \frac{\int \left(\bar{v}\left(\mathbf{x}\right)-v\right)^2\,\alpha(\mathbf{x},v)\,dv}{\int \alpha(\mathbf{x},v)\,dv}. \tag{5}$$

The denominator ensures proper normalization of α, whose integral over v is not necessarily equal to 1. Assuming normally distributed diffraction information around the expectation velocity allows us to construct our second weight, $W_2(\mathbf{x},v)$:

$$W_2(\mathbf{x},v) = \frac{\exp\left(-\frac{(\bar{v}(\mathbf{x})-v)^2}{2\sigma_v^2(\mathbf{x})}\right)}{\int \exp\left(-\frac{(\bar{v}(\mathbf{x})-v)^2}{2\sigma_v^2(\mathbf{x})}\right)dv}. \tag{6}$$

We construct our final weight, $W_3(\mathbf{x},v)$ using the observation that properly migrated diffractions are focused, or localized in space, and therefore the magnitude of the spatial derivative of semblance normalized by the value of semblance at that location should change rapidly in the vicinity of properly migrated diffractions:

$$W_3(\mathbf{x},v) = \frac{||\nabla_{\mathbf{x}}\alpha(\mathbf{x},v)||_2}{\alpha(\mathbf{x},v)}. \tag{7}$$

More weights may be used by eager practitioners able to determine other attributes correlated to diffraction likelihood, but seeking a simplification, we content ourselves with three. Thus, for m weights enumerated by j, and allowing $\tilde{I}(\mathbf{x},v) = \int I(\mathbf{x},v,p)\,dp$, we may calculate our probabilistic diffraction image as:

$$\widehat{I}(\mathbf{x}) = \int \tilde{I}(\mathbf{x},v)\prod_{j=1}^{m} W_j(\mathbf{x},v)\,dv. \tag{8}$$

Note that the weights we have constructed (and the combined weights) are pseudo-probabilities with the exception of W_2. They do not have all the properties of a true probability function, as that would imply that a diffraction must occur within a region in space. Rather, these weights show a general tendency for whether or not diffractions are likely to occur. Because W_2 is a probability of a velocity being accurate, and intuitively we assume that there must exist an accurate migration velocity at every point in space, we may build that weight so it fulfills the criteria of a probability.

METHODOLOGY

We illustrate our probabilistic diffraction imaging method on a toy model (Landa et al., 2008; Klokov and Fomel, 2013; Decker et al., 2017a). Figure 1 features a chart with the workflow for the imaging process. Note that when comparing this chart to the figures of the toy model, the vector $\mathbf{x}$ in the chart corresponds to $[t, x]$ in the toy model example. The order of arguments for objects in the chart and toy model may differ, as the order of arguments in figure labels correspond to the order axes are displayed in the figure. The toy model contains one reflector dipping downward to the right, a single point diffractor centered beneath 0.5 km and a planar reflector with a constant velocity of 1.0 km/s. Zero-offset data are modeled and displayed in Figure 2.

The process of OVC is applied to the data and their slope-decomposed images are propagated through a range of migration velocities to create a series of slope decomposed partial images. Slices through this volume are illustrated in Figure 3. The front panes of box plots in this figure display slope gathers centered at 0.5 km, directly above the diffractor, for three different migration velocities. The right right panes show the image created by stacking over slope for the selected migration velocity. Notice that for all three velocities, energy corresponding to the reflectors, near 2.1 s and 4 s, bend upward in the slope gathers. The lowest point in the upward bending reflection energy corresponds to the slope of that reflector. Notice that this apex is achieved at greater time values with higher migration velocities for the dipping reflector, and that the slope corresponding to this apex is greater for higher migration velocities. This is because migration makes dipping events steeper, and migration with larger velocities further increases the slope of dipping events. Diffraction energy in the left panel bends upward in a "smile" indicating under-migration. The energy flattens in the middle panel corresponding to correct migration. In the right panel it bends downward in a "frown" indicating over-migration. As we will see, the flat, correctly migrated diffraction energy results in a semblance high. Examining the stacked continuation images on the right panes of the box plots, we see that the diffraction bows downward when undermigrated in the left panel, is focused into a point when properly migrated in the center panel, and bows upward when overmigrated in the right panel. The slope of the dipping reflector increases with increased velocity, while the flat reflector's slope and vertical position is unaffected.

The creation and application of probabilistic weights to partial images images to

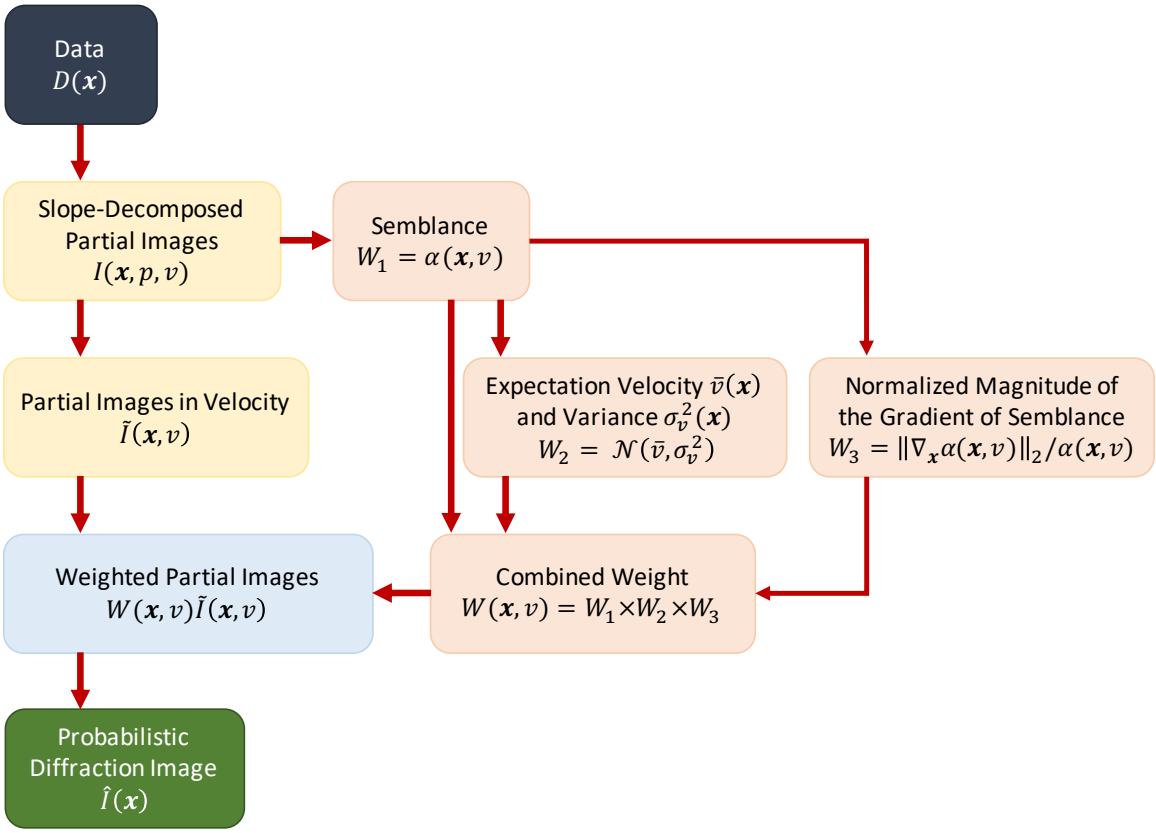

Figure 1: Probabilistic diffraction imaging workflow

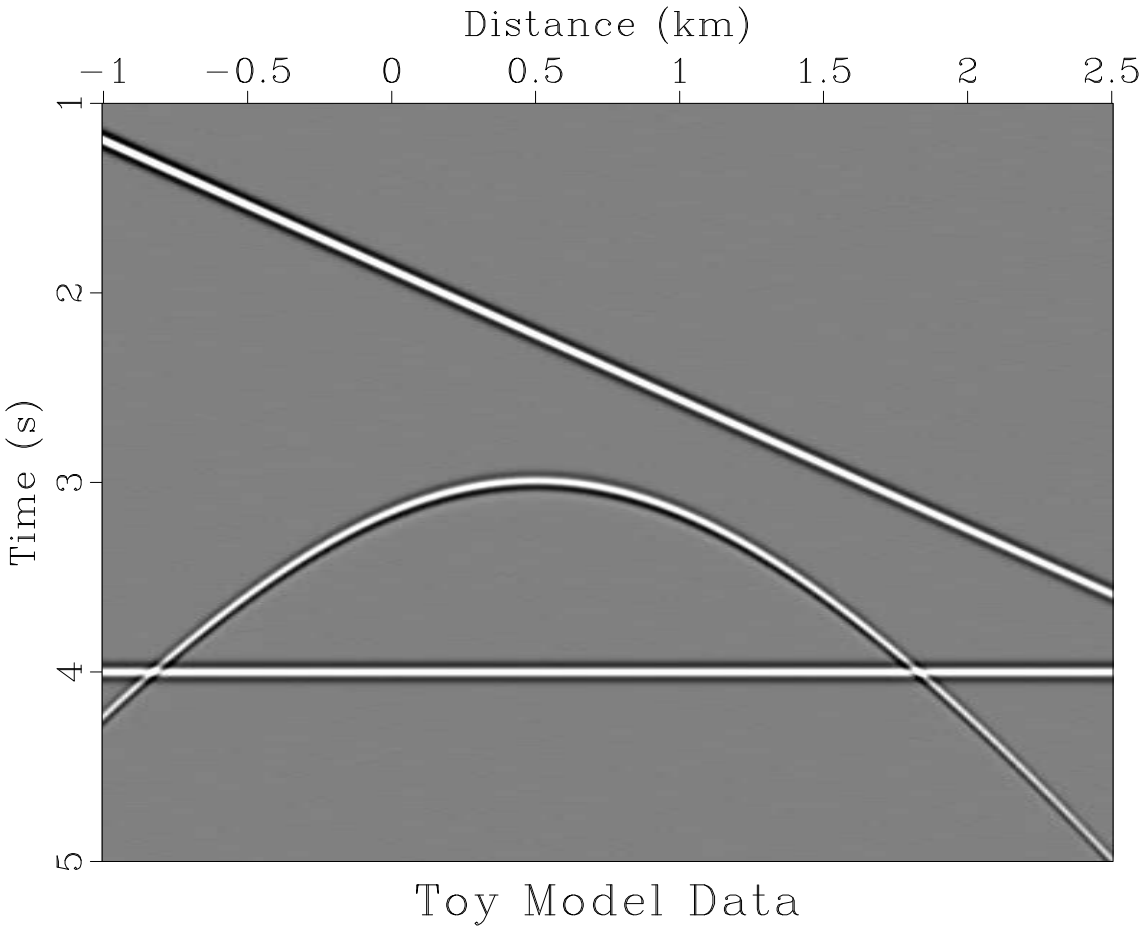

Figure 2: Toy model data containing two reflectors and a point diffractor.

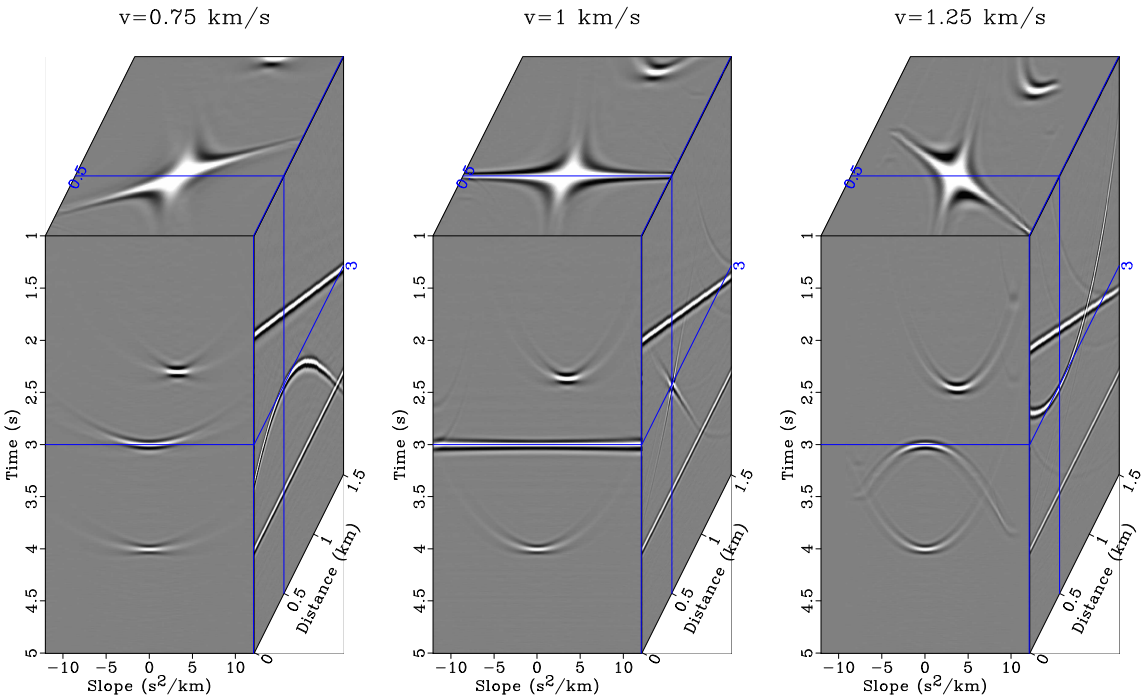

Figure 3: Example of application of OVC to toy model for three continuation velocities: left panel is under-migration with 0.75 km/s; central is for 1.0 km/s, the correct velocity; right is over-migration with 1.25 km/s. Front face of box plots show slope gathers centered above the diffraction. Right face of box plots show the image that results from stacking over slope gathers for that continuation velocity.

create a probabilistic diffraction image is illustrated in Figure 4. The front pane of the top left box in Figure 4 contains a partial image in velocity generated by stacking the OVC output over slope at 0.5 km, centered directly above the diffractor, while the side pane shows the slice through this continuation volume for a velocity of 1 km/s, which corresponds to a deterministic image with the true migration velocity.

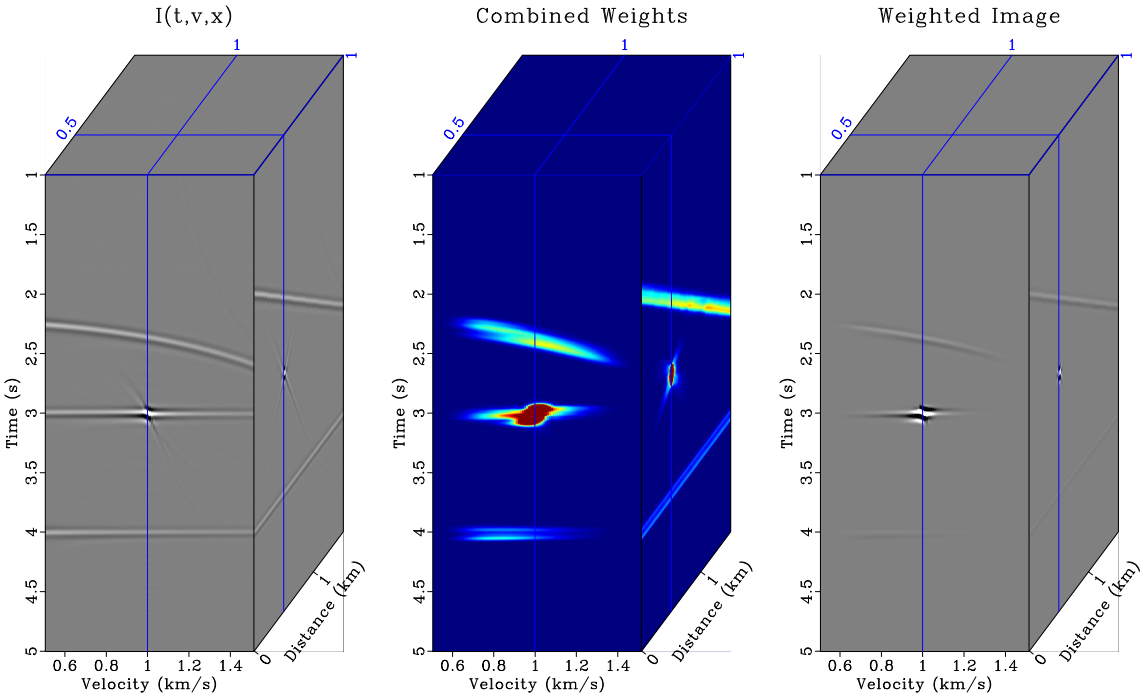

Figure 4: Probabilistic migration process illustrating the action of weights on $I(t, v, x)$ for the toy model, with the front panes of box plots centered at $x = 0.5$ km, directly over the diffractor. The top left box contains an output $I(t, v, x)$ volume that results from stacking the output of OVC over slope. Top middle box contains the combined weights that the top left box will be multiplied by. Top right box shows the image on the left multiplied by the combined weights. Bottom left box contains W_1, the image semblance. Bottom middle box contains W_2, a weight normally distributed around expectation velocity using its variance. Bottom right box plots W_3, a weight based on the relative magnitude of semblance's gradient.

For this section we calculate the three imaging weights, shown in the bottom row of Figure 4. The bottom left box contains W_1, the image semblance calculated according to Equation 3. Semblance provides a measure of when slope-gathers are flat, and thus semblance highs can indicate where diffractions have been migrated using the correct velocity. Using this semblance, the expectation velocity, $\bar{v}$, and its variance, σ_v^2, are calculated according to Equations 4 and 5. A normal distribution is fit to that velocity and variance according to Equation 6, generating W_2 which is plotted in the lower middle box.

Notice that $\bar{v}$, the expectation velocity, occurring at the maximum value of W_2,

does not track the true velocity, 1 km/s in the shallow or deep portions of the panel. This is because diffraction data does not exist there to be utilized for maximizing semblance. However, $\bar{v} \approx 1$ km/s at 3 s, where the diffraction takes place. The lower right box displays W_3, a weight based on how quickly semblance, or W_1 , changes in space.

The three weights in the lower row of Figure 4 posses high values at the time and position of the diffraction at the correct migration velocity but they are also non-zero at other locations where diffraction did not occur. The top middle box of Figure 4 shows how multiplying the three weights together further emphasizes the region of the partial image with diffraction data. Multiplying this combined weight by the input $I(t, v, x)$ in the top left box of Figure 4 generates the weighted partial image on the top right box of that Figure. Notice how the energy of the diffraction at the correct velocity is emphasized, while other energy present is suppressed.

We generate a suite of images to compare different imaging methods. Figure 5a contains an "ideal image" generated by convolving the toy model reflectivity with a 10 Hz peak frequency Ricker wavelet. Figure 5b contains the deterministic image created through migration with the correct velocity. Figure 5c contains an equal weight comparison image, constructed in the manner of the equal weight images featured in Merzlikin and Fomel (2017). This is the equivalent of stacking the top left box of Figure 4 over velocity for each midpoint. Figure 5d contains our probabilistic diffraction image, generated by stacking the weighted images shown in the top right box of Figure 4 over velocity for every midpoint. It is the output of Equation 8.

To highlight the wavefield components contributing to each of these images we generate a series of slope gathers centered above the diffractor at 0.5 km. Stacking each of these gathers over slope would create the traces at 0.5 km in their corresponding images. Figure 6a contains an "ideal gather" generated by warping the ideal image in Figure 5a to squared time, decomposing it into constituent slope components, and warping the slope decomposed image back to time. The plane wave destruction slope calculated from the ideal image warped to squared time is plotted on this gather with fuchsia x's where reflectors are present. Figure 6b contains a gather contributing to the deterministic image, Figure 5b. This gather is generated by selecting $I\left(t, x, v_{mig}, p\right)$ for $v_{mig} = 1.0$ km/s. Figure 6c contains a gather corresponding to the equal weight image, Figure 5c. It is constructed by stacking the slope decomposed partial images in velocity,$I\left(t, x, v, p\right)$, over velocity. Figure 6d contains a gather corresponding to the probabilistic diffraction image, Figure 5d. It is generated by multiplying the combined weights and the slope decomposed partial images in velocity and stacking over velocity.

As one would expect, the ideal image in Figure 5a features excellently focused and easily discernible diffraction and reflection events. The diffraction in this image is marked by a well defined single point without features radiating away from that point – the point spread function is not present for the diffractor, as the Hessian corresponding to modeling and migration has not been applied to this image. Examining the gather centered at 0.5 km for this image, Figure 6a, the most visible

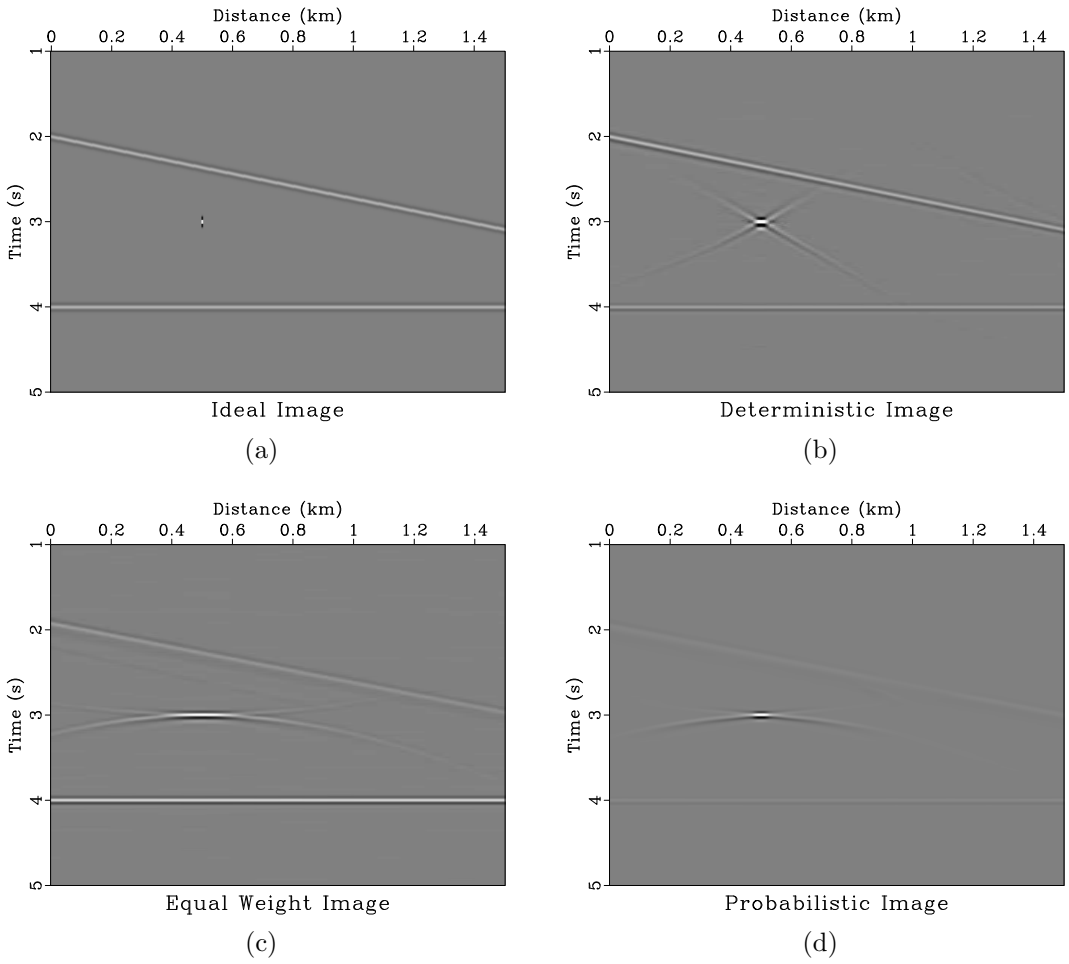

Figure 5: Comparison of probabilistic diffraction imaging output with other methods: (a) ideal image corresponding to the toy model reflectivity convolved with a 10 Hz peak frequency Ricker Wavelet; (b) deterministic image created by migrated the data in Figure 2 using its migration velocity, 1 km/s; (c) equal weight image generated by stacking $I(t, x, v, p)$ over v and p using equal weights; (d) the probabilistic diffraction image.

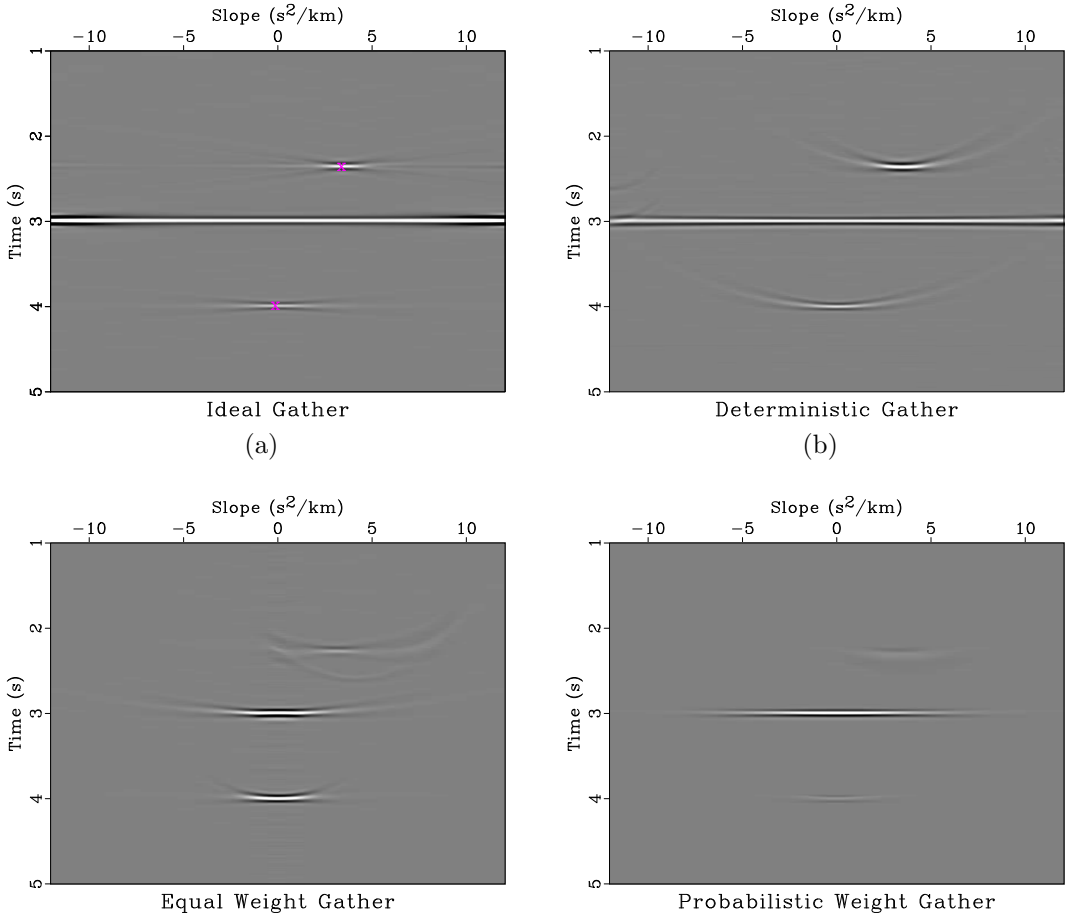

Figure 6: Slope gathers centered at 0.5 km, directly above the diffractor, corresponding to the: (a) ideal image, Figure 5a overlaid by slope denoted using fuchsia x's where reflectors are present; (b) deterministic image, Figure 5b; (c) equal weight image, Figure 5c; (d) the probabilistic diffraction image, Figure 5d.

feature is the energetic flat diffraction event extending across all slopes in the gather. One may think of two equivalent reasons for why diffraction energy appears this way in slope gathers. The first is because a point contains information from all slopes – one may see this by taking the fk transform of a dot. The second is that if we think of an idealized diffraction hyperbola extending to infinity, that hyperbola will contain all slopes, from asymptotically vertical up to the right, to flat at the point of the diffractor, to asymptotically vertical downward to the right. Migration with the correct velocity collapses diffraction hyperbolas to a point. Thus a properly migrated idealized diffraction will contain information from all slopes transformed to the same point in space, and such a diffraction in a slope gather immediately above the diffractor would appear as a flat event extending over all slopes. In practice, even in synthetic experiments, seismic data does does not contain such idealized diffraction hyperbolas extending to infinity due to limited spatial geophone or receiver coverage, so only a portion of slopes contribute to the diffraction image. This effect is visible in the point spread function, appearing like a "bow tie". The two reflectors are also visible in this ideal gather, featuring energy confined to a narrower range of slopes centered about the observed slope for each reflector, noted by fuchsia x's. This is intuitive, because planar reflection events contain energy from their dominant slope.

The deterministic image in Figure 5b appears similar to the ideal image in Figure 5a with an added "bow tie" point spread function around the diffractor. This result is unsurprising – it assumes complete apriori information about the subsurface velocity field. Differences with the ideal image are caused by the incomplete spatial sampling of the wavefield. Examining the gather corresponding to this image, Figure 6b shows that as was the case in the ideal gather, three clearly defined events are visible correlating to the two reflections, each centered at their corresponding slope, and the diffraction event. As is expected in such a synthetic experiment, the reflection and diffraction events for this deterministic gather generated using the correct migration velocity appear quite similar to those in the ideal gather. A minor difference between the two gathers is the appearance of upward bowing energy around reflection events in the deterministic gather, which is absent from the ideal gather. Also, notice that energy corresponding to the diffraction event increases for large amplitude slope values in the ideal gather, but remains relatively constant in the deterministic gather. This is a result of the slope decomposition used to generate the ideal gather placing diffraction energy for slopes larger than those present in the gather at those large slope values. A true "ideal gather" of a diffraction would have slopes extending to infinity and feature constant energy for all slope values.

In the equal weight image, Figure 5c, the flat reflector is imaged quite well, as all its energy is stationary at the correct time. The dipping reflector appears more smeared because the time its energy achieves the stationary apex in Figure 3 changes with velocity, and thus interferes destructively on stacking in this imaging method. The stationary remaining energy corresponds to that of the initial and final velocities, which have no lower or higher velocities respectively to interfere destructively with. This is evident in the gather corresponding to the equal weight image, Figure 6c, where two weak events corresponding to the dipping reflector are visible. The upper

event is related to migration with the initial velocity, and the weaker, lower event is related to migration with the greatest velocity considered. This type of behavior can also be seen in the equal weight diffraction featured in Figure 5c. Rather than having a artifact around the diffraction corresponding to limited spatial coverage, as was the case in Figure 5b, here there is an artifact around the diffraction corresponding to only considering a limited set of migration velocities prior to stacking. Two events, a stronger one bowing downward which is an imprint left by undermigration of diffraction energy with the initial velocity, and a weaker upward bowing event corresponding to diffraction overmigration appear. If we performed this experiment using a dense sampling of velocities spanning all positive numbers, these artifacts would not be present. Diffraction energy is less well spatially resolved than in Figure 5b, appearing more laterally spread out.

The probabilistic diffraction image, Figure 5d successfully highlights diffraction energy and suppresses energy corresponding to reflectors. A "bow tie" point spread function similar to that appearing in Figure 5b is not present in this image, although there is a minor artifact appearing like a weaker version of the one surrounding the diffraction in Figure 5c. The diffraction in Figure 5d has similar lateral resolution to that in Figure 5b and superior resolution to Figure 5c. Examining the gather corresponding to the probabilistic diffraction image, Figure 6d, shows that although energy corresponding to the two reflection events is present, it is dramatically reduced compared to the deterministic gather in Figure 6b. This illustrates why the method is intended to be used on data where diffraction extraction has already been attempted – although reflection suppression has occurred it is not complete, so applying the method to complete data featuring both strong reflections and diffractions would not generate ideal results. However, this suppression is complementary to any data-domain reflection removal that occurs before applying the approach, for example using plane-wave destruction. Diffraction energy in the probabilistic gather appears flat, resembling the diffraction energy in the "ideal gather" of Figure 6a and the deterministic gather of Figure 6b, although the slope coverage of the probabilistic gather is more limited than those two. This is because diffraction energy present at large slopes is more responsive to velocity perturbation than those at small slopes, so destructive interference from partial images in velocity near the true migration velocity which receive a non-zero weight in the probabilistic imaging process suppress diffraction energy at these slope values.

SYNTHETIC EXAMPLE

We illustrate the function of the probabilistic diffraction imaging method and its robustness to noise on a synthetic model consisting of random diffractions in a constant velocity gradient media recreated from Decker et al. (2017a).

Figure 7 contains 24 offsets of modeled diffraction data with no added noise. Diffraction data are slope decomposed and OVC is performed over a range of plausible migration velocities. As was the case for the toy model example, we generate

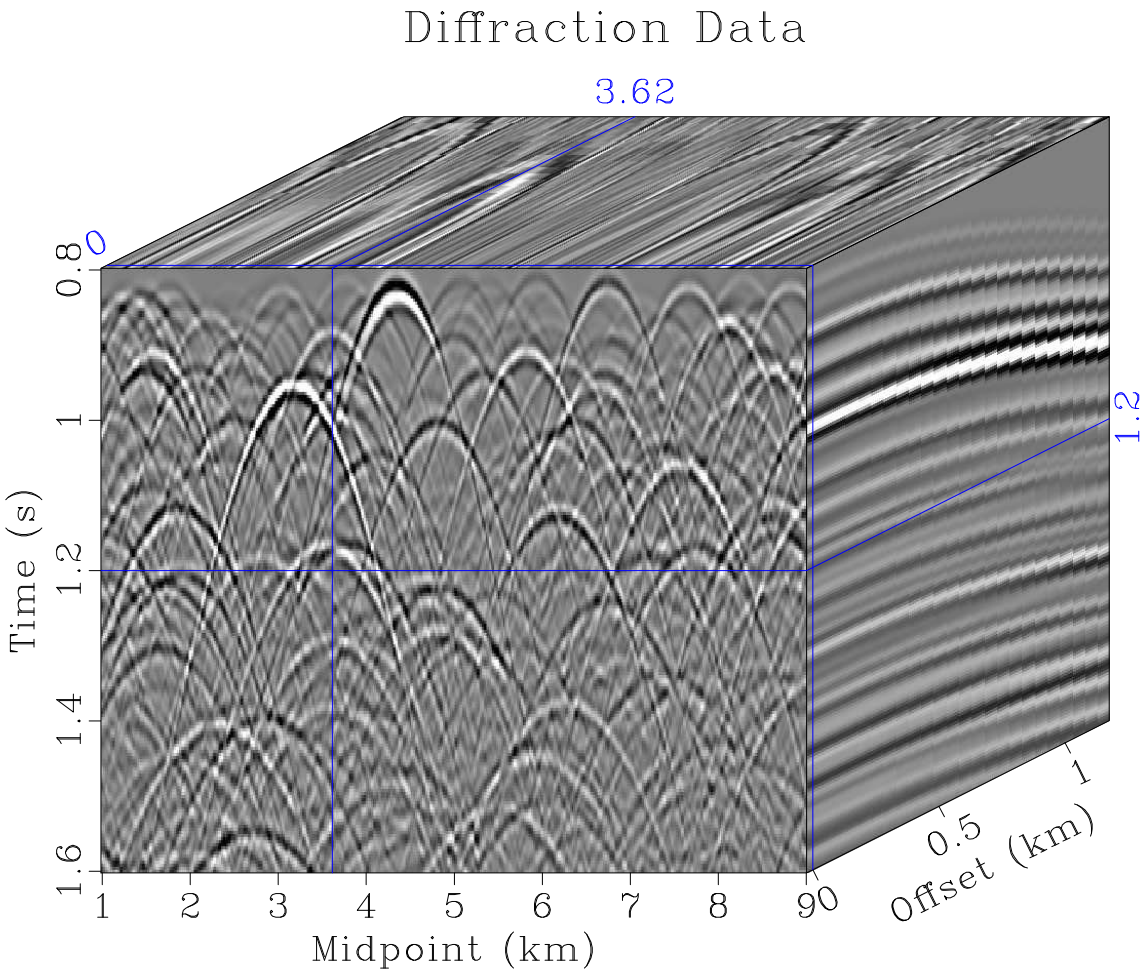

Figure 7: Synthetic dataset consisting of diffractions in constant velocity gradient media modeled for 24 offsets with a 50 m increment.

partial images and weights as a function of continuation velocity for each midpoint. This process is illustrated for gathers centered below 3.62 km in Figure 8. The top left box plot of Figure 8 contains partial images in velocity generated by stacking the OVC output, $I(\mathbf{x}, v, p)$ over slope, p. The lower row of Figure 8 shows the weights that will be applied to that partial image. The lower left box plot contains W_1, the image semblance calculated according to Equation 3. Using this semblance, the expectation velocity, $\bar{v}$, and its variance, σ_v^2, are calculated according to Equations 4 and 5. A normal distribution is fit to that velocity and variance according to Equation 6, generating W_2 as shown in the lower middle box plot. Although $\bar{v}$, the expectation velocity, does not always completely track the true velocity, it is always within one standard deviation. Expectation velocity tends to drift away from the true velocity in the shallow portion of the synthetic, which could be explained by the fact that the shallowest diffractions in the model occur at 0.8 s. Thus, less information is available in the shallow portion to guide the expectation velocity. The right box plot displays W_3, a weight based on how quickly W_1 changes in space.

The three weights are multiplied together to provide the top center box plot of Figure 8, the combined weight. Multiplying the partial images in the top left box plot of Figure 8 by this combined weight provides the weighted partial images shown on the right box plot.

As was the case with the toy model example used in the methodology section, we generate a suite of images to compare imaging methods on this noiseless synthetic. Figure 9a shows an ideal image of this synthetic model consisting of the reflectivity model convolved with a 50 Hz peak frequency Ricker wavelet. Figure 9b contains the deterministic image created using migration with the correct velocity. Figure 9c contains an equal weight path integral image generated by stacking the partial images in the top left box plot of Figure 8 over velocity for each midpoint. Figure 9d contains our probabilistic diffraction image, generated by stacking the weighted partial images shown in the top right box plot of Figure 8 over velocity for every midpoint.

We also create a series of gathers to illustrating the contribution of different wavefield components to the images. Stacking each of these gathers over slope creates the traces at 3.62 km in their corresponding images. Figure 10a contains an "ideal gather" generated by warping the "ideal image" in Figure 9a to squared time, decomposing it into constituent slope components, and warping the slope decomposed image back to time. Figure 10b contains a gather contributing to the deterministic image, Figure 9b. This gather is generated by selecting $I\left(t, x, v_{mig}, p\right)$ for the true migration velocity. Figure 10c contains a gather corresponding to the equal weight image, Figure 9c. It is constructed by stacking the slope decomposed partial images in velocity, $I\left(t, x, v, p\right)$ over velocity. Figure 10d contains a gather corresponding to the probabilistic diffraction image, Figure 9d. It is generated by multiplying the combined weights and the slope decomposed partial images in velocity and stacking over velocity.

In this noiseless example, the deterministic image in Figure 9b is unsurprisingly able to image most of the diffractions in the ideal image, Figure 9a. This is because

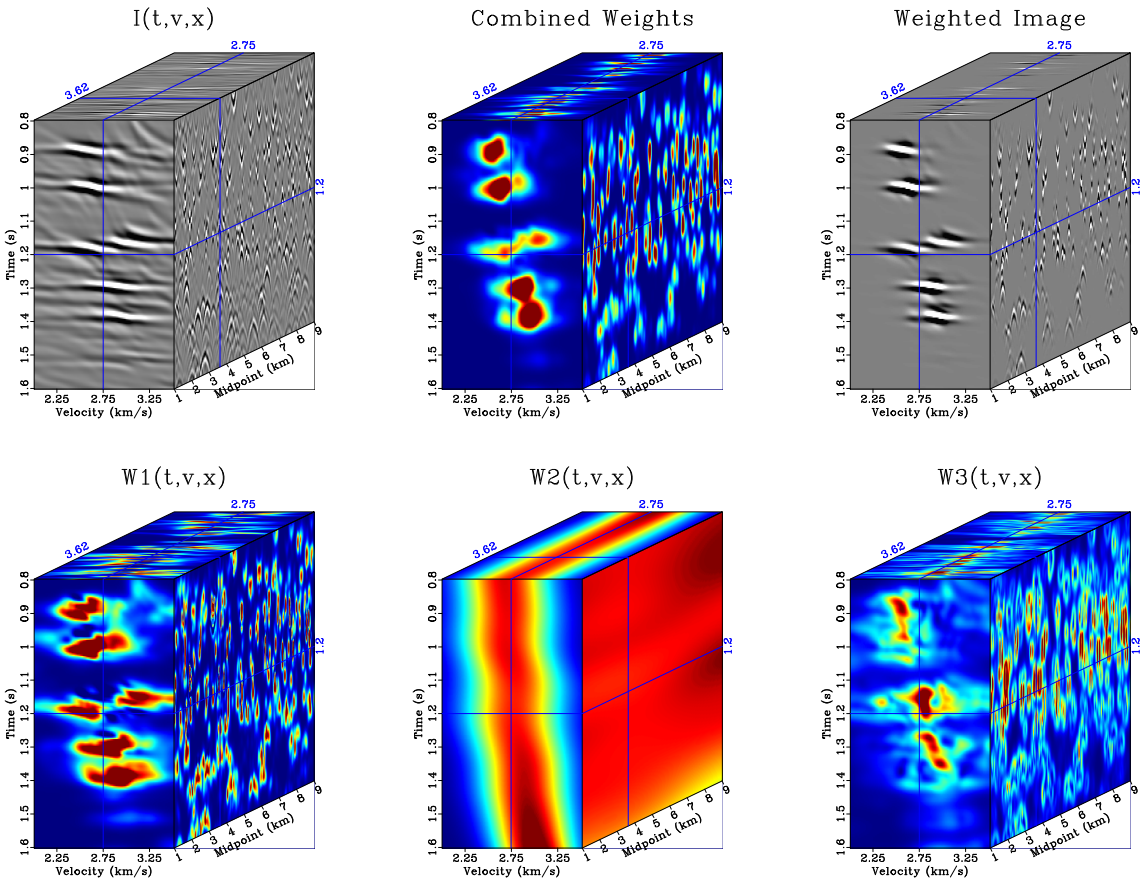

Figure 8: Illustration of the probabilistic diffraction imaging process on $I(x, t, v)$ for a gather at centered 3.62 km for the noiseless synthetic. Top left box plot contains partial images output by the OVC process. Top middle box plot contains the combined weights that the left panel will be multiplied by. Top right box plot shows the partial images on the left multiplied by the combined weights. Bottom left box plot shows W_1, the image semblance. Bottom middle box plot contains W_2, a weight normally distributed around expectation velocity, $\bar{v}$, using the expectation velocity's variance, σ_v^2. Bottom right box plot has W_3, a weight based on the relative magnitude of semblance's gradient.

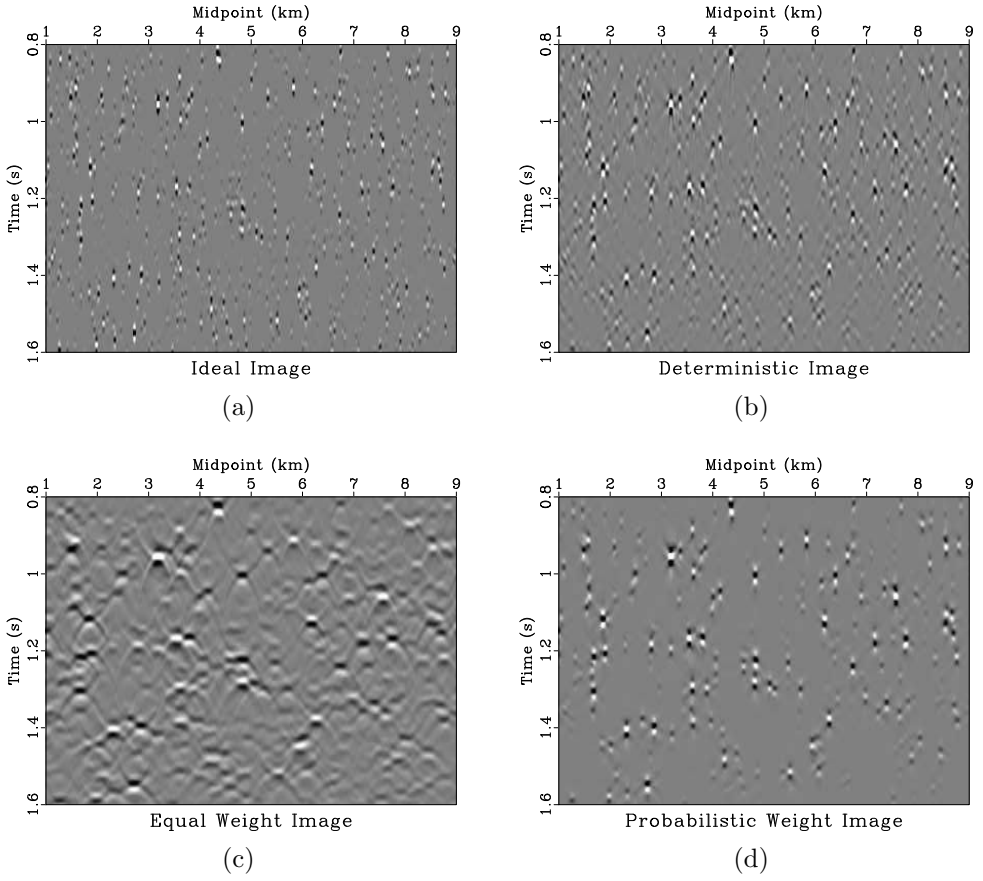

Figure 9: Noiseless synthetic model imaging comparison: (a) ideal image consisting of synthetic model reflectivity convolved with a 50 Hz peak frequency Ricker wavelet; (b) deterministic image created by migrating the noiseless synthetic data using its true velocity; (c) equal weight path integral image generated by stacking $I(t, x, v, p)$ over v and p using equal weights; (d) probabilistic diffraction image generated by stacking $I(t, x, v, p)$ over v and p using probability weights.

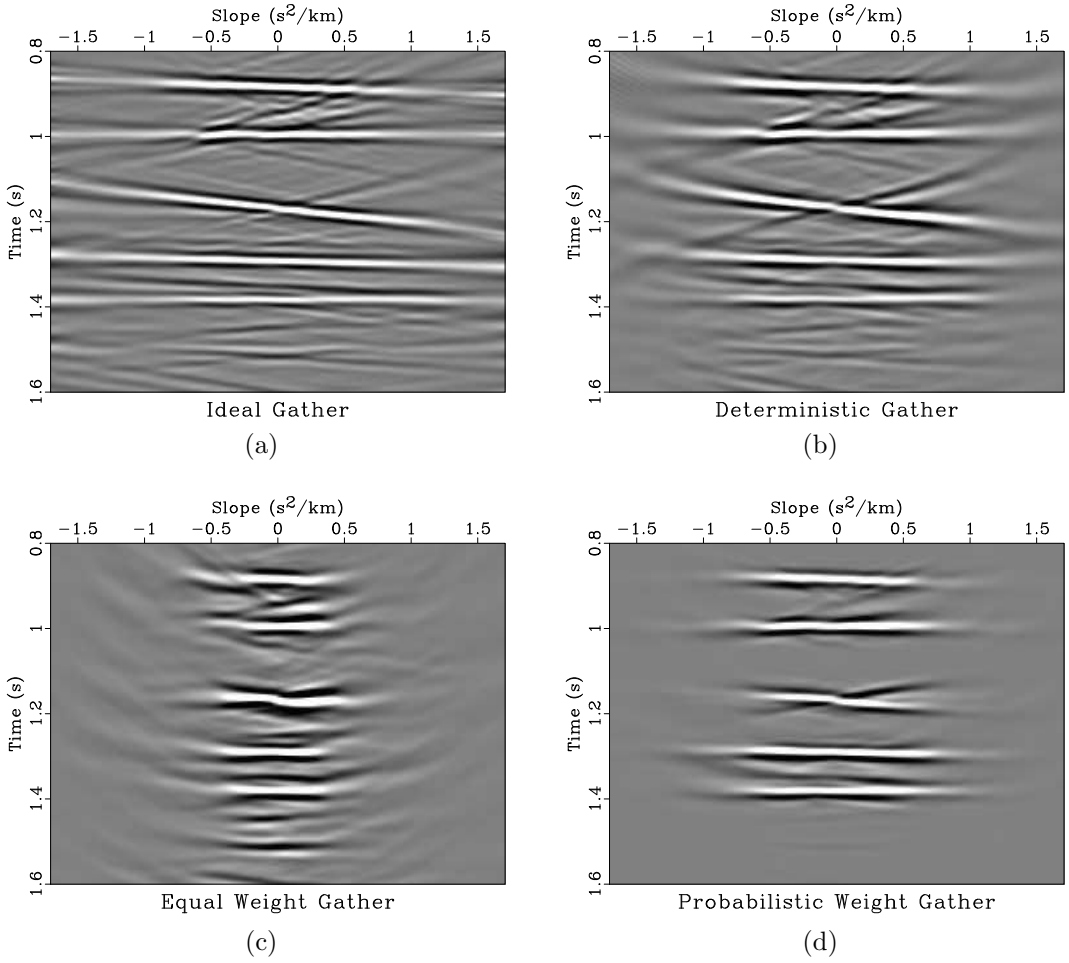

Figure 10: Slope gathers centered at 3.62 km for the noiseless synthetic corresponding to the: (a) ideal image, Figure 9a; (b) deterministic image, Figure 9b; (c) equal weight image, Figure 9c; (d) the probabilistic diffraction image, Figure 9d.

in this example, the deterministic imaging process receives perfect apriori knowledge of the subsurface velocity field, so it would be expected to be extremely effective at imaging diffractions. Notice that in the process of modelling and migration, the dynamic range of diffractions appears to be amplified in the deterministic image relative to the ideal image, which consists of the reflectivity model convolved with a wavelet. Diffractions which are weak in the ideal image appear weaker in the deterministic image, and strong diffractions appear stronger. An example of this behavior is in the cluster of weak diffractions around 1.55 s between 3 and 4 km, which are relatively more energetic and better resolved in Figure 9a than Figure 9b. The deterministic image also has slightly poorer lateral resolution of diffractions than the ideal image. The deterministic gather, Figure 10b appears similar to the ideal gather in Figure 10ak although energy is primarily confined to slopes between -1 and 1 s^2/km. Energy in these gathers that is flat corresponds to diffractions immediately below the gather. Energy that is sloping correlates to diffractions away from the gather's midpoint. The greater the slope of energy in the gather, the further away the event is. For example, the sloping event centered around 1.15 s in the ideal gather, Figure 9a, corresponds to a strong diffraction event occurring around 1.15 s below 3.5 km, slightly to the left of this gather which is centered at 3.62 km. Only diffraction events events that are nearly flat in these gathers will be stationary upon stacking. The sloping events will interfere destructively with themselves, as is the case with the sloping event centered around 1.15 s, which does not appear in the ideal image at 3.62 km, although some energy is present there in the deterministic image, Figure 9b because diffractions in that image are less spatially focused and thus wider.

The equal weight image, Figure 9c, resolves many of the diffractions visible in the ideal image, Figure 9a but with significantly reduced spatial resolution. The increase in dynamic range visible in the deterministic image, Figure 9b is also visible here, and often diffractions which are separate in the ideal image appear merged in the equal weight image. It is often difficult to discern individual weak diffraction events in this image. Examining the equal weight gather, Figure 10c, notice that the range of slopes where energy is present is more limited, typically ranging between -0.5 and 0.5 s^2/km. Much of the sloping energy associated with diffractions centered beneath different midpoints which is visible in Figures 10a and 10b is absent here. Because the equal weight image has poorer lateral resolution than the ideal or deterministic images, several diffraction events which are centered nearby appear as flat diffraction energy in the equal weight gather, but appear as sloping events in the deterministic or equal weight gathers. Two examples of this occur at approximately 1.45 and 1.55 s. Note that although the equal weight image does not resolve diffraction events as well as the deterministic image, it was not the recipient of apriori knowledge of the subsurface velocity field during the imaging process.

The probabilistic diffraction image, Figure 9d effectively focuses the energy of moderate to strong diffractions. Diffractions seen in the probabilistic image have better spatial resolution than those in the equal weight image. Although some weak diffractions that are present in the ideal image of Figure 9a and the deterministic image of Figure 9b, recall that unlike the deterministic image, the probabilistic im-

age did not receive apriori knowledge of the subsurface velocity field to use during imaging. Instead, such a field was output during the creation of probability weights. Examining the gather corresponding to the probabilistic image, Figure 10d, notice that the gather has a cleaner appearance. Energy present in the probabilistic gather spans a similar range of slopes to that of the deterministic gather, roughly -1 to 1 s^2/km. Events visible in the probabilistic weight gather tend to be the flat ones indicative of a diffraction at that location. Sloping events corresponding to diffractions at other midpoints tend to be suppressed. This is because the weights are primarily based on semblance, a measure of gather coherence. Thus, the method amplifies the nearly flat coherent events possessing high semblance values. The use of weights tied to coherence explains why some weak diffractions can be suppressed in the imaging process. This synthetic model possesses dense field of diffractions, as is visible in the diffraction data of Figure 7. The moveout curves associated with these diffractions frequently intersect, which leads to the phenomenon of sloping energy corresponding to diffractions centered at a different midpoint intersecting the flat energy in a gather corresponding to a diffraction located at that midpoint. The resulting superposition of sloping and flat energy is less laterally coherent, and thus will have a lower semblance value than if the sloping energy was not present. The effect becomes stronger when the coherent flat event is similarly or less energetic to intersecting events. This behavior can be seen in gently sloping events below 1.4 s in the four gathers. Although these events slope more gently than the event at 1.15 s, their superposition is laterally incoherent. Because the probabilistic imaging process amplifies events that are laterally coherent in these gathers, which is a typical feature of diffractions, they are dramatically suppressed.

We repeat the synthetic experiment adding 10-60 Hz band passed Gaussian noise to the diffraction data following modeling to show the robustness of the probabilistic imaging method to noise. The added noise is strong, it has a RMS value approximately 16.5 times greater than that of the noiseless diffraction data from the initial part of this experiment. Noisy zero offset data are shown in Figure 11. We perform OVC and again illustrate the probabilistic imaging process in Figure 12. The top left box plot of Figure 12 contains partial images output by OVC after stacking over slope. The slope-decomposed images output by OVC are also used to calculate the weight functions shown in the bottom row of Figure 12. In order to suppress unreasonable values, tapered muting is applied to W_1 before calculating the other weights. The three weights are multiplied together to create the combined weight shown in the top middle box plot of Figure 12. Multiplying the combined weight by the partial images in the left box plot creates the weighted partial images in the top right box plot of Figure 12.

As with the noiseless example, we generate a suite of images to compare imaging methods. Figure 13a shows an ideal image of this synthetic model consisting of the reflectivity model convolved with a 50 Hz peak frequency Ricker wavelet. This image is the same as that in Figure 9a as we used the same model and wavelet. Figure 13b contains the deterministic image created using migration with the correct velocity. Figure 13c contains an equal weight path integral image generated by stacking the

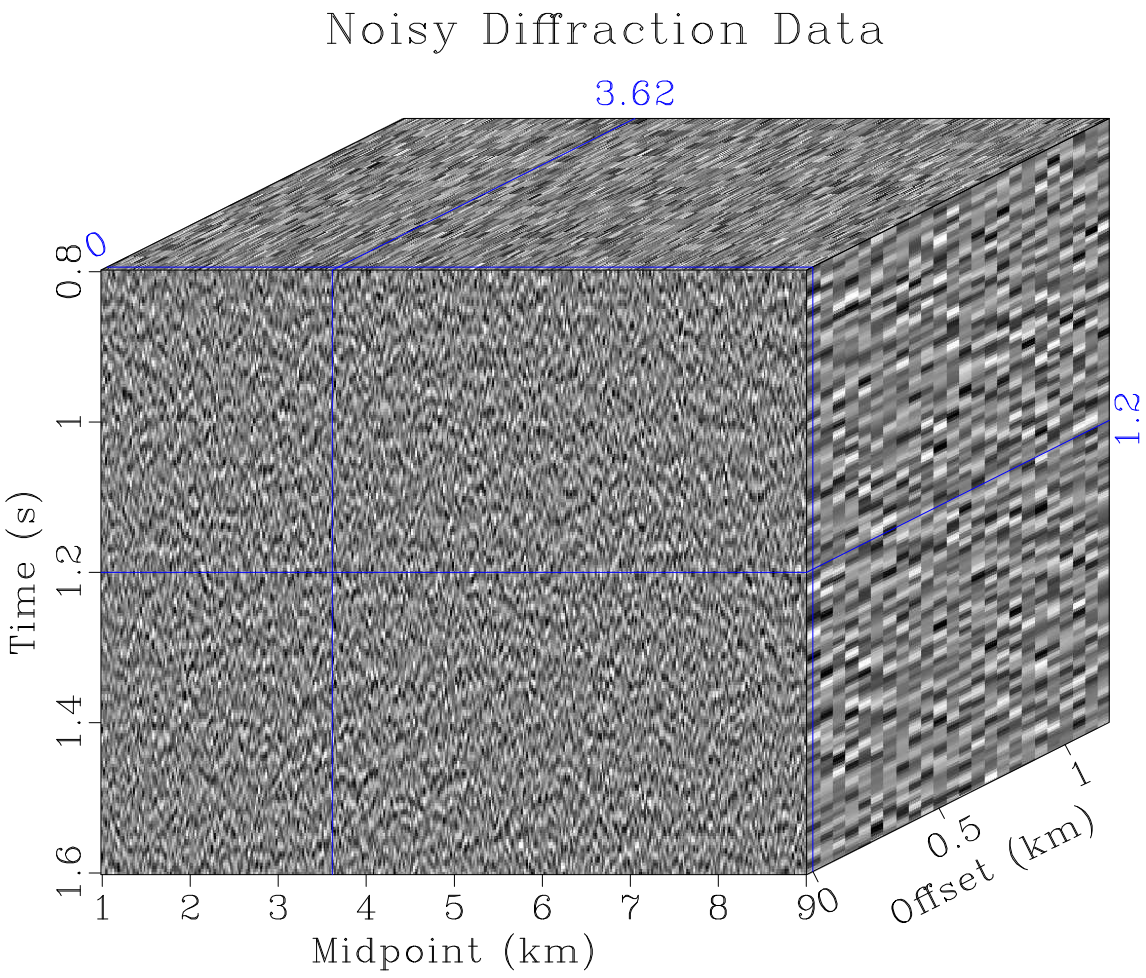

Figure 11: Synthetic dataset consisting of diffractions in constant velocity gradient media modeled for 24 offsets with a 50 m increment from Figure 7 with band passed Gaussian noise added.

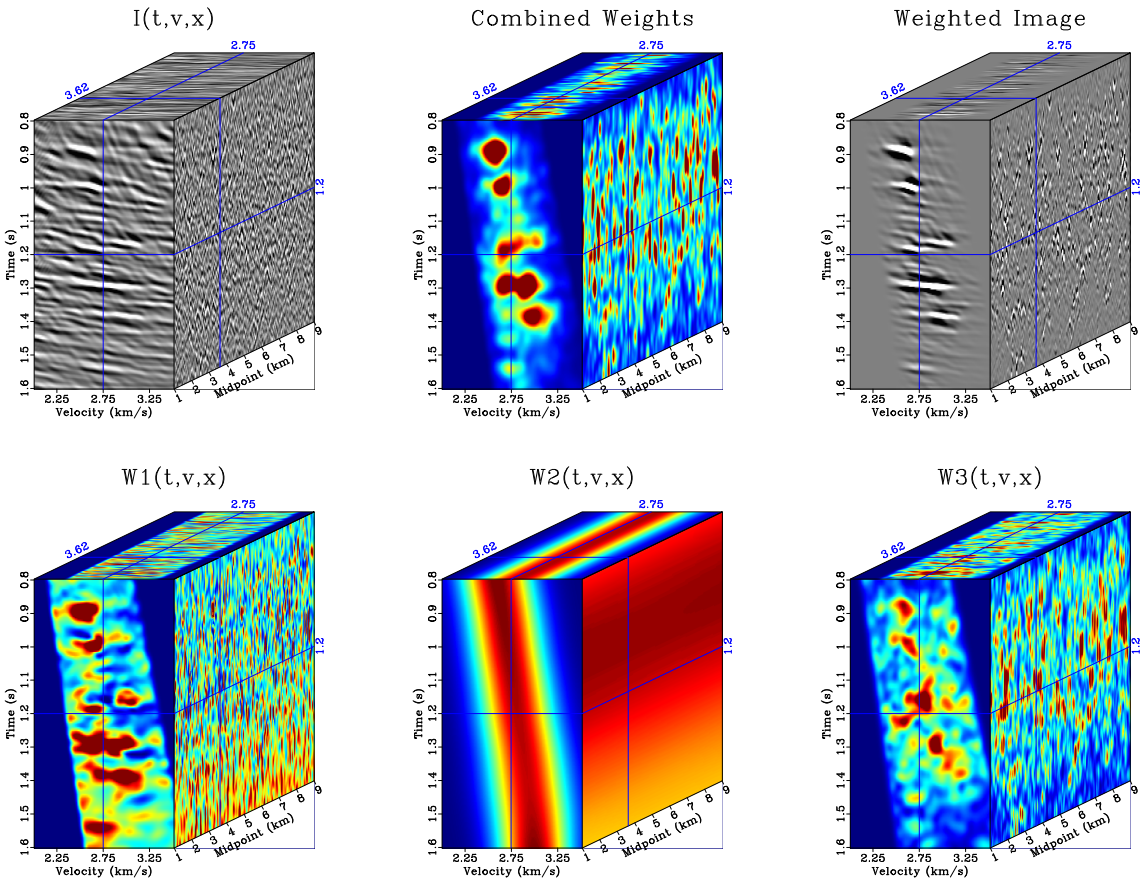

Figure 12: Illustration of the probabilistic diffraction imaging process on $I(x, t, v)$ for a gather at centered 3.62 km for the noisy synthetic. Left box plot contains partial images output by the OVC process. Central box plot contains the combined weights that the left panel will be multiplied by. Right box plot shows the partial images on the left multiplied by the combined weights. Bottom left box plot shows W_1, the image semblance. Bottom middle box plot contains W_2, a weight normally distributed around expectation velocity, $\bar{v}$, using the expectation velocity's variance, σ_v^2. Bottom right box plot has W_3, a weight based on the relative magnitude of semblance's gradient.

partial images in the top left box plot of Figure 12 over velocity for each midpoint. Figure 13d contains our probabilistic diffraction image, generated by stacking the weighted partial images shown in the top right box plot of Figure 12 over velocity for every midpoint.

We similarly create a series of gathers to illustrating the contribution of different wavefield components to the noisy images at the same midpoint location as the gathers in the noiseless example, 3.62 km. Figure 14a contains an ideal gather generated by warping the ideal image in Figure 13a to squared time, decomposing it into constituent slope components, and warping the slope decomposed image back to time. As was the case with the ideal image, this ideal gather is the same as that in Figure 9a. Figure 14b contains a gather contributing to the deterministic image, Figure 13b. This gather is generated by selecting $I\left(t, x, v_{mig}, p\right)$ for the true migration velocity. Figure 14c contains a gather corresponding to the equal weight image, Figure 13c. It is constructed by stacking the slope decomposed partial images in velocity, $I\left(t, x, v, p\right)$ over velocity. Figure 14d contains a gather corresponding to the probabilistic diffraction image, Figure 13d. It is generated by multiplying the combined weights and the slope decomposed partial images in velocity and stacking over velocity.

The noisy deterministic image, Figure 13b, contains significantly more noise than its noiseless counterpart, Figure 9b. Although some of the strongest diffractions seen in the ideal image, Figure 13a can be seen in the deterministic image, it can be difficult to tell which objects are diffractions and which are noise without the ideal image as reference. The corresponding deterministic gather, Figure 14b is also noisy when compared to the ideal gather, Figure 14a. As was the case with the deterministic image, although most of the planar diffraction events from the ideal gather can be seen in the deterministic gather and identified because of their lateral coherence, their amplitudes are typically not much stronger than those of background noise.

The noisy equal weight image, Figure 13c, is corrupted by noise. Few diffractions can be discerned in the image, and it is difficult to say with certainty what features are diffractions and what are simply high amplitude noise. This behavior is reflected in the corresponding equal weight gather, Figure 14c, which contains numerous high amplitude events not present in the noiseless equal weight gather, Figure 10c.

The probabilistic diffraction image shown in Figure 13d is resilient to noise, featuring most of the diffractions visible in Figure 9d. Background noise, though present, is not as powerful as the strong diffractions, and is significantly suppressed relative to the noisy deterministic and equal weight images. Features in the probabilistic weight gather, Figure 14d appear more laterally coherent and less noisy than those in the deterministic or equal weight gathers, signifying that the energy present is far more likely to be caused by diffraction. Indeed, comparing this noisy probabilistic weight gather to the noiseless one in Figure 10d shows that most events appearing in the noisy gather have corresponding events in the noiseless one. Also note that the noisy deterministic image received perfect apriori knowledge of underlying velocity to use in the migration process, while this probabilistic image did not.

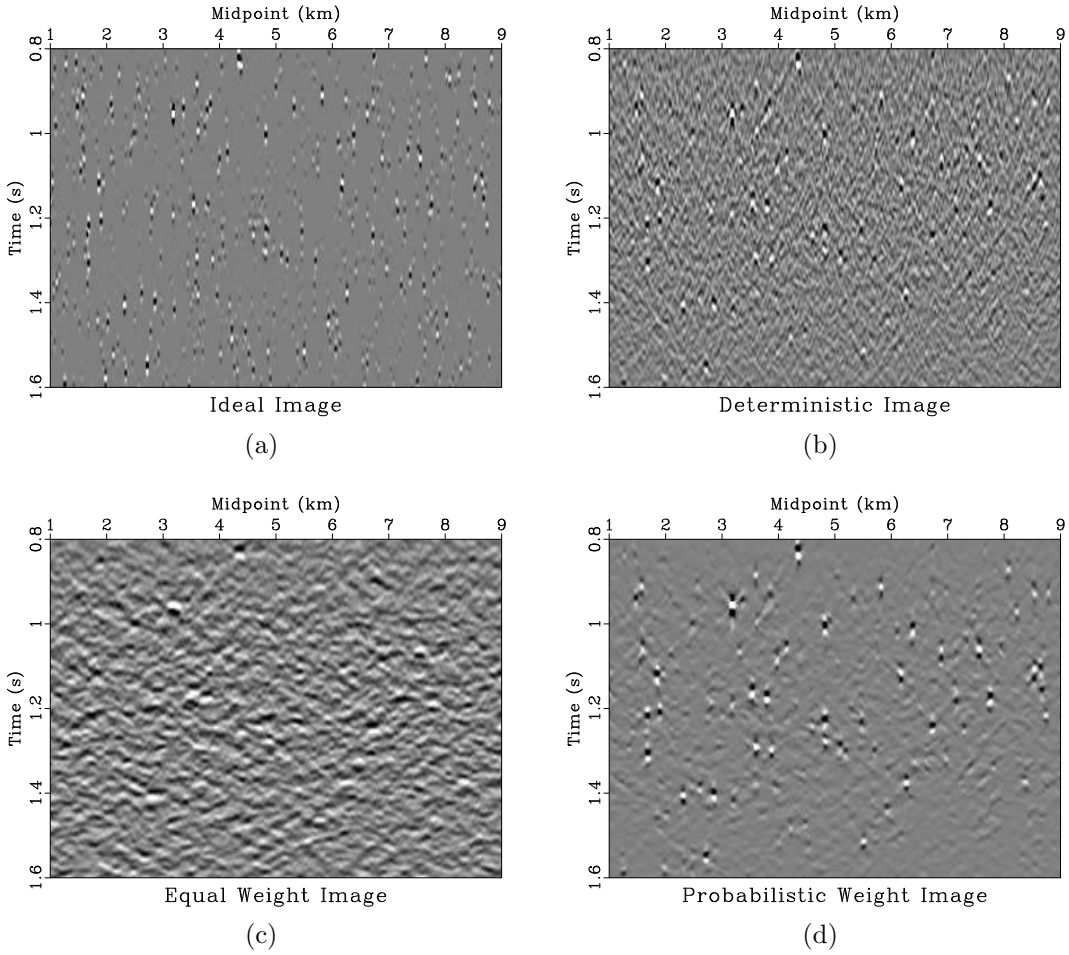

Figure 13: Noisy synthetic model imaging comparison: (a) ideal image consisting of synthetic model reflectivity convolved with a 50 Hz peak frequency Ricker wavelet; (b) deterministic image created by migrating the noiseless synthetic data using its true velocity; (c) equal weight path integral image generated by stacking $I(t, x, v, p)$ over v and p using equal weights; (d) probabilistic diffraction image generated by stacking $I(t, x, v, p)$ over v and p using probability weights.

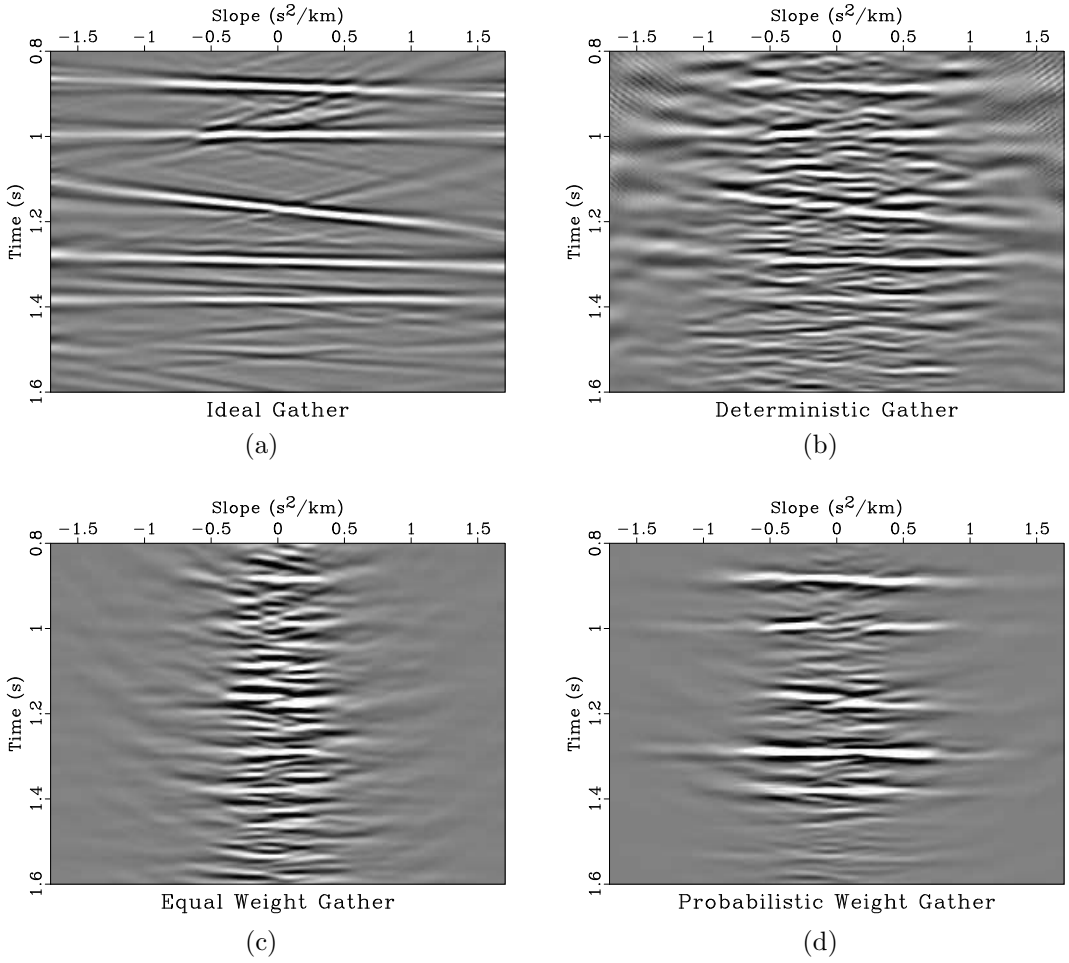

Figure 14: Slope gathers centered at 3.62 km, directly above the diffractior corresponding to: (a) ideal image, Figure 13a; (b) deterministic image, Figure 13b; (c) equal weight image, Figure 13c; (d) the probabilistic diffraction image, Figure 13d.

FIELD DATA EXAMPLE

We apply our method to a 2D deepwater field dataset acquired to image the Nankai Trough subduction zone in Japan off the shore of Honshū in the Philipine Sea, where the Philipine Plate subducts below the Eurasian Plate. Moore et al. (1990) contains relevant data acquisition parameters and processing results associated with this dataset, which is referred to as NT62-8. Moore and Shipley (1993) performed structural interpretation on the line. Additional regional context may be found in Moore et al. (2007) and Bangs et al. (2009). This experiment examines CMPS 900-1301 from that line, previously used by Forel et al. (2005) and Decker et al. (2017a). This portion of the line highlights the transition from trench, stretching to to the south, or off to the left of our study area with lower CMP numbers, to a highly deformed accretionary wedge of sedimentary rocks featuring numerous thrust faults that overlays the subducting oceanic crust within our study area. This dataset features numerous diffractions, making it well suited for application to diffraction imaging.

Data are pre-processed by correcting traces to be zero-mean, using a 10-125 Hz bandpass filter, applying surface consistent amplitude correction, and resampling to 4 ms. Data are then DMO stacked, shown in Figure 15a, and diffractions are extracted through plane-wave destruction (Fomel et al., 2007). Diffraction data are displayed in Figure 15b. OVC is performed on the diffraction data from Figure 15b, outputting a suite of slope-decomposed diffraction images for 60 different migration velocities, beginning at 1.4 km/s with a 20 m/s increment.

Slope-decomposed images are used to perform the probabilistic diffraction imaging process, illustrated in Figure 16. Stacking the slope-decomposed partial images, $I(t, v, x, p)$ over slope p provides the partial images in the top left box plot of Figure 16. Semblance is calculated from slope-decomposed partial images according to Equation 2, and is used to generate the imaging weights shown in the bottom row of Figure 16 as well as the expectation velocity and its variance, plotted in Figures 17a and 17b respectively.

Multiplying the weights together provides the combined weight in the top middle box plot of Figure 16. Multiplying those weights by the partial images in velocity in the top left box plot generates the weighted partial images in the top right box plot. We use the expectation velocity in Figure 17a to generate a deterministic complete image, shown in Figure 18a. We generate a deterministic diffraction image plotted in Figure 18b by migrating the diffraction data in Figure 15b using the expectation velocity in Figure 17a, and a equal weight diffraction image, Figure 18c by stacking the partial images in the upper left box plot of Figure 16 over velocity with equal weights. Stacking the weighted partial images in the upper right panel of Figure 16 over velocity provides the probabilistic diffraction image in Figure 18d.

We generate a suite of slope gathers for midpoints at 4100 m to illustrate how different wavefield components contribute to the four images. Figure 19a contains a slope gather corresponding to the Nankai Trough complete image, Figure 18a. That gather is overlaid by a fuchsia plot of image slope at that midpoint computed by

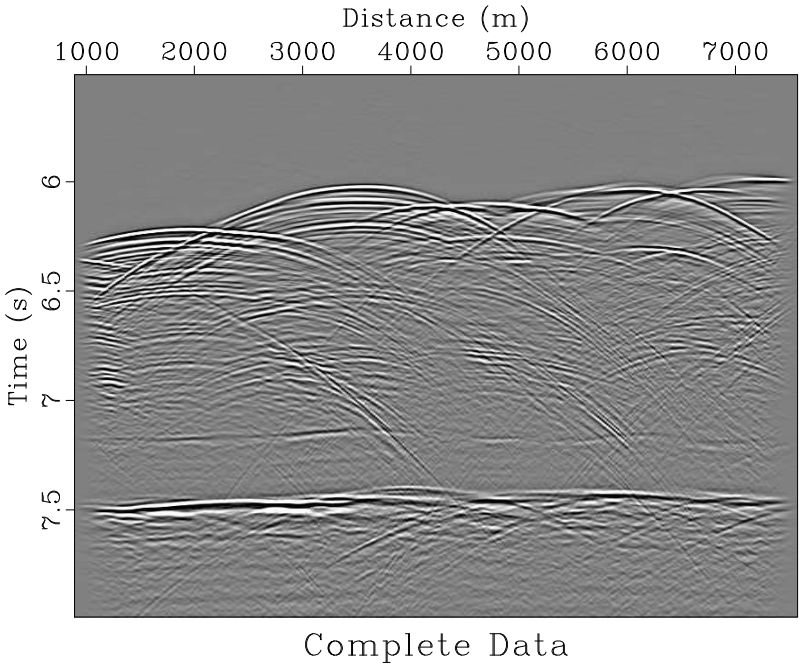

Complete Data

(a)

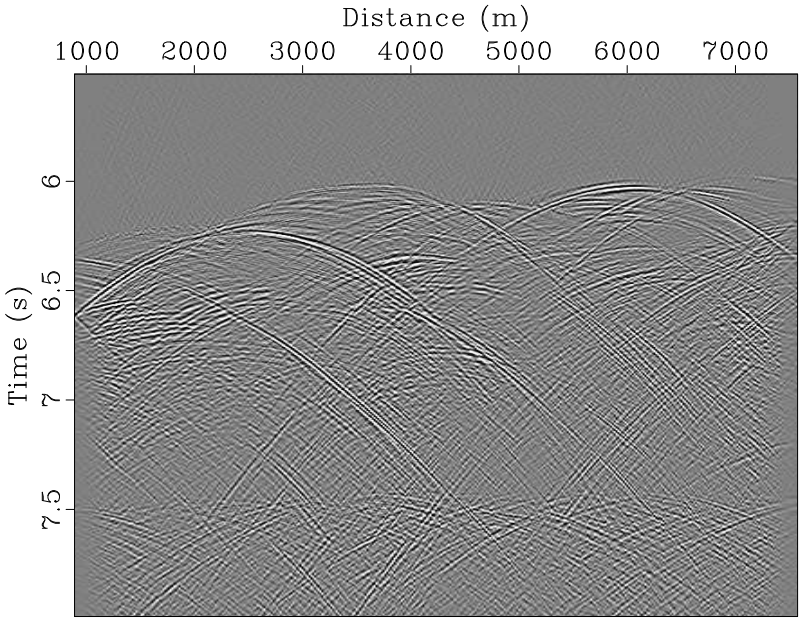

Diffraction Data

(b)

Figure 15: Field data from Nankai Trough: (a) complete data; (b) plane-wave destruction diffraction data.

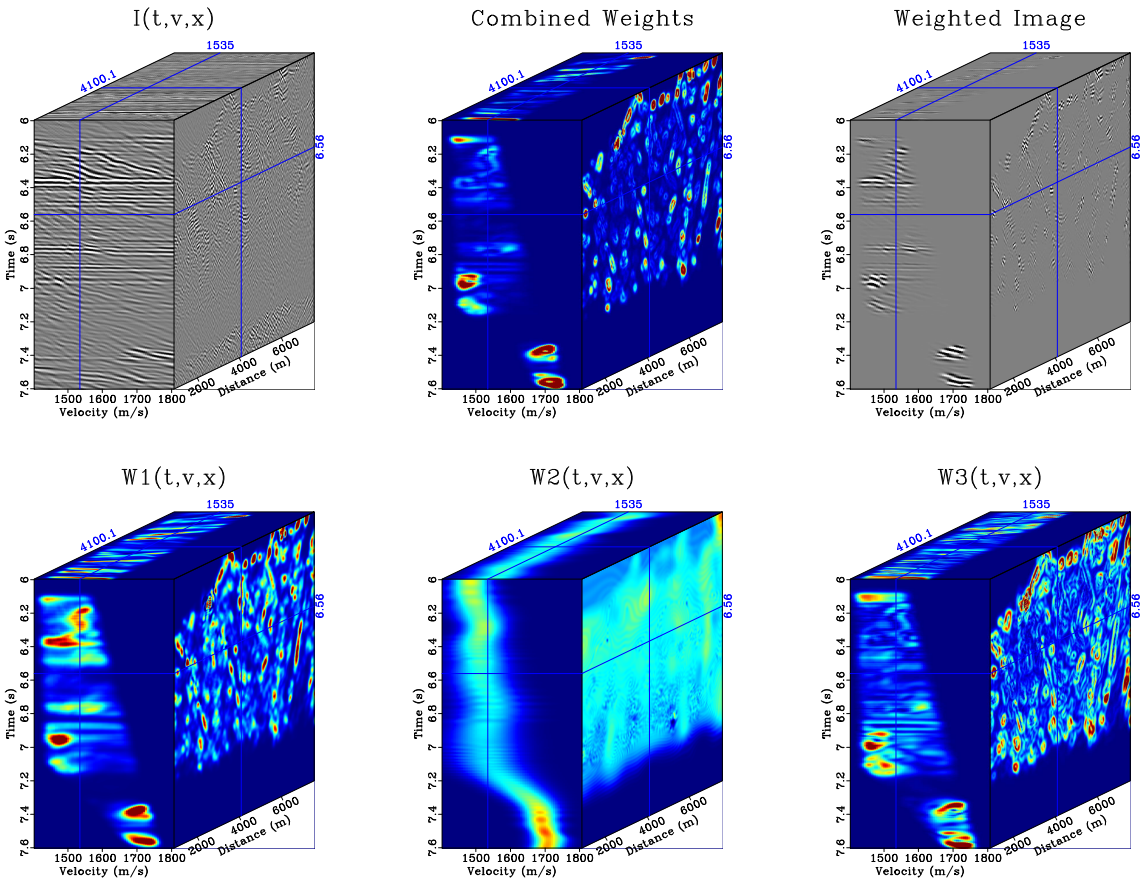

Figure 16: Illustration of the probabilistic diffraction imaging process on the Nankai field dataset on a gather centered at Distance 4100 m: Top left box plot contains partial images output by the OVC process after stacking over slope. Top middle box plot contains the combined weights that the left panel will be multiplied by. Top right box plot shows the partial images on the left multiplied by the combined weights. Bottom left box plot shows W_1, the image semblance. Bottom middle box plot contains W_2, a weight normally distributed around expectation velocity, $\bar{v}$, using the expectation velocity's variance, σ_v^2. Bottom right box plot has W_3, a weight based on the magnitude of semblance's gradient.

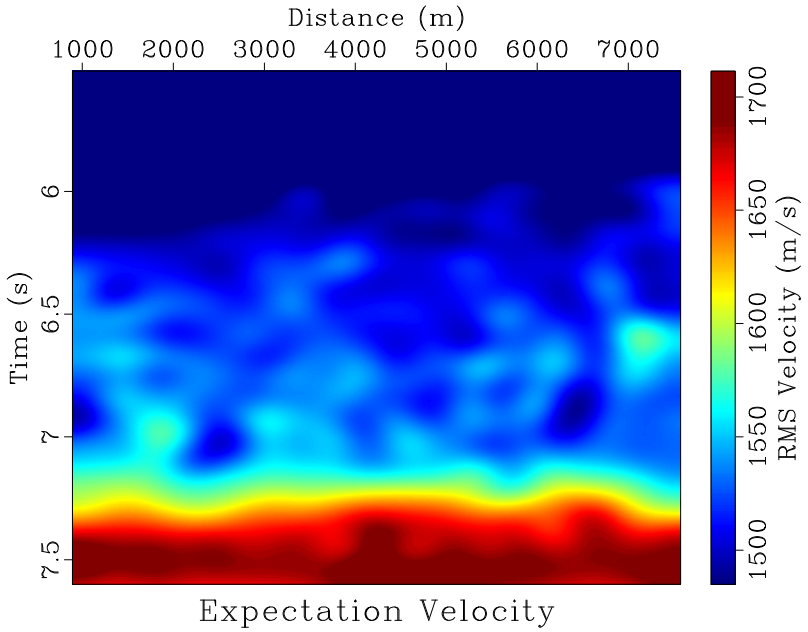

(a)

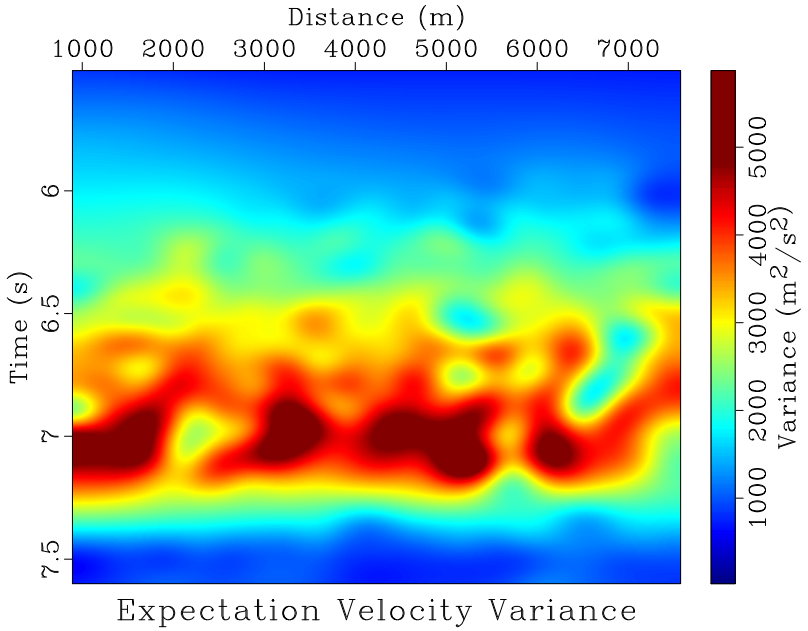

(b)

Figure 17: Nankai Trough velocity attributes calculated from semblance: (a) expectation velocity; (b) velocity variance.

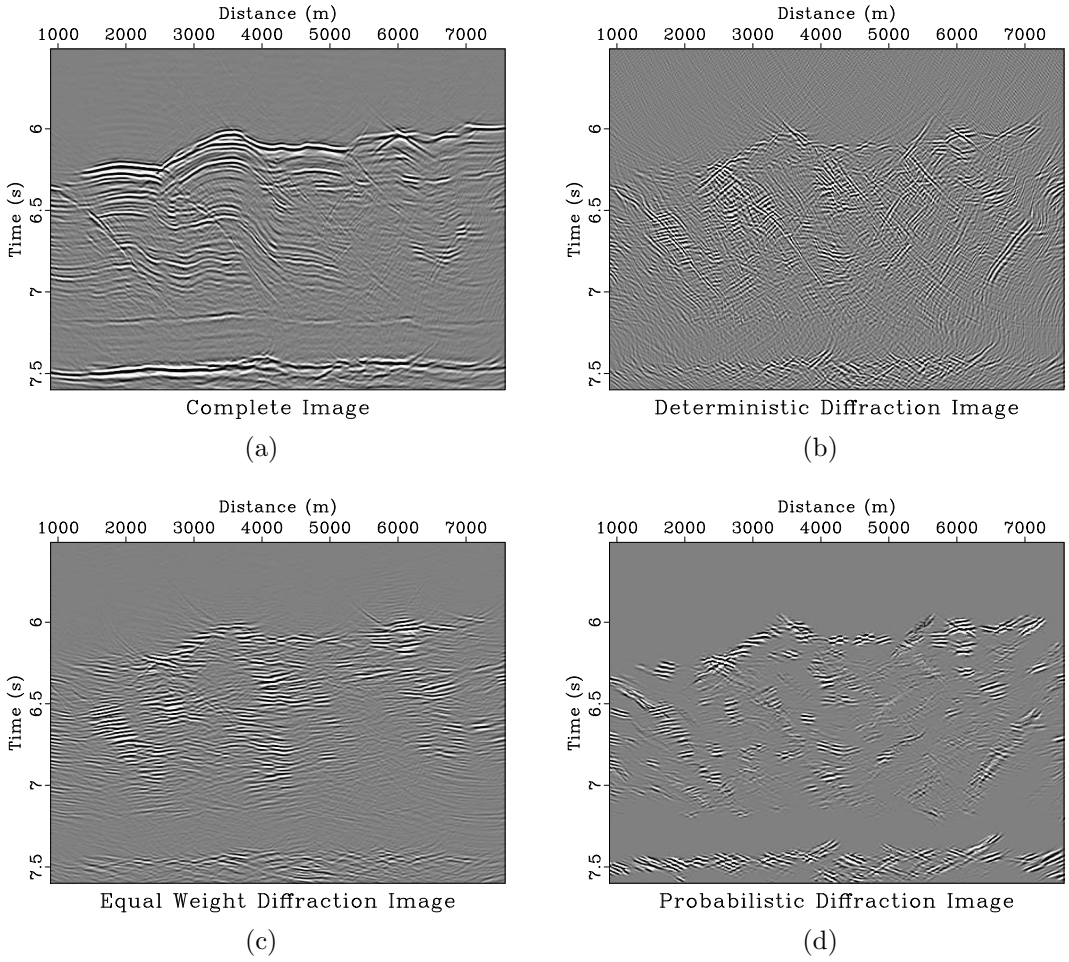

Figure 18: Images of the Nankai Trough: (a) deterministic complete image generated by migrating the complete data in Figure 15a using the expectation velocity, Figure 17a; (b) deterministic diffraction image generated by migrating the diffraction data, Figure 15b, using the expectation velocity, Figure 17a; (c) diffraction image generated through the equal weight stack over velocity of the the partial images in the left box plot of Figure 16; (d) probabilistic weight diffraction image created by stacking the weighted partial images in the top right box plot of Figure 16 over velocity.

warping the complete image to squared time, determining slope, and then warping that slope back to non-squared time following the same process used in the toy model example to find the slope plotted in Figure 18a. Figure 19b displays the slope gather corresponding to the deterministic diffraction image, Figure 18b, Figure 19c features the gather corresponding to the equal weight image, Figure 18c, and Figure 19d has the gather corresponding to the probabilistic diffraction image, Figure 18d.

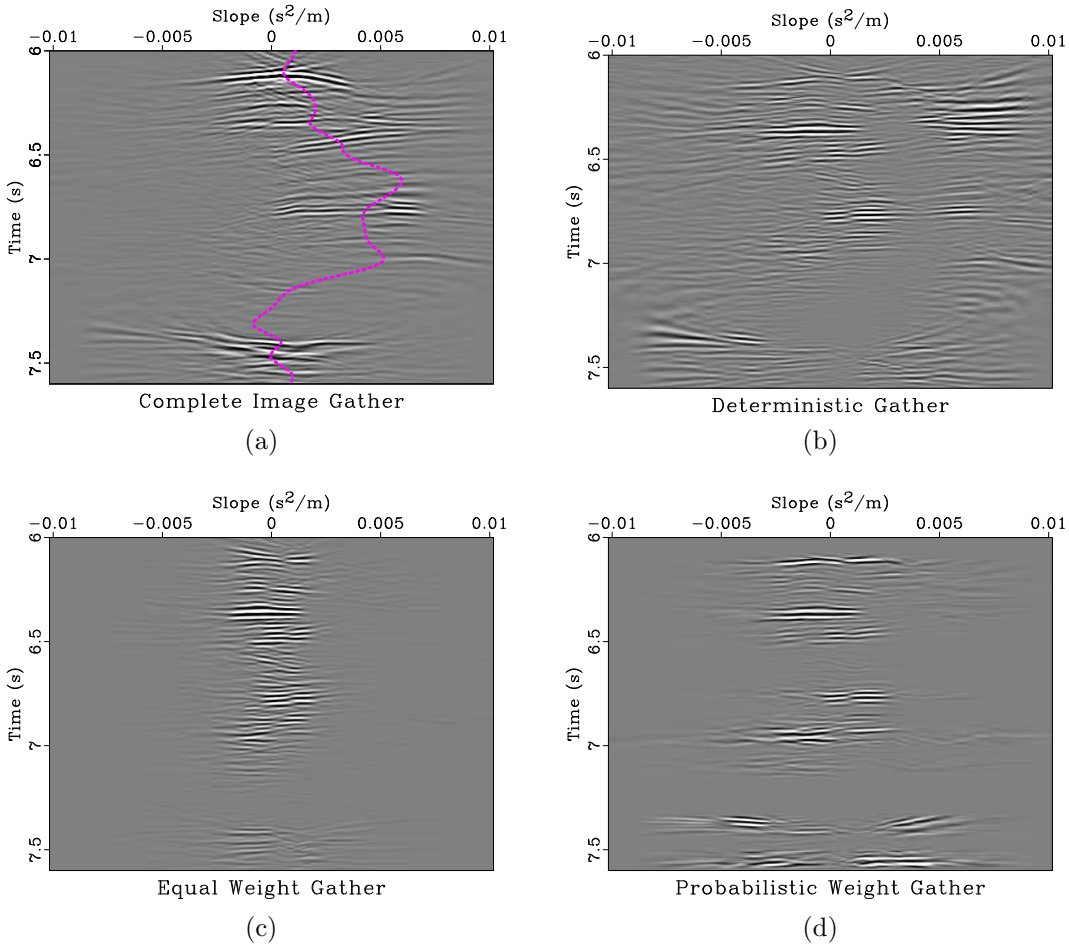

Figure 19: Slope gathers centered at 4100 m corresponding to (a) the complete image, Figure 18a; (b) the deterministic diffraction image, Figure 18b; (c) the equal weight image, Figure 18c; (d) the probabilistic diffraction image, Figure 18d.

The probabilistic weight diffraction image better highlights diffractive features and suppresses remnant reflection signal than the deterministic or equal weight diffraction images. Diffractions delineating the seafloor between about 5.9 and 6.3 s, and likely tied to slumps, are well resolved in the probabilistic diffraction image, but less defined in the deterministic and equal weight images where they are either less focused or overwhelmed by their point spread functions and noise, making it more difficult to discern the location of the seafloor.

Diffractions highlighting thrust faults, particularly two that intersect the seafloor

at 1000 km and 2300 km and extend downward to the right to a relatively flat décollement extending laterally at about 7.2 s and defining the plate boundary, are clearly visible in the probabilistic diffraction image. These faults are more difficult do distinguish in the deterministic diffraction image due to remnant reflections and in the equal weight diffraction image due to background noise.

A highly diffractive layer extending laterally at about 7.5 s marking the transition from sedimentary to crystalline rock is more localized in the probabilistic diffraction image than the deterministic or path integral diffraction images. This boundary marks the deepest diffractions observed in this data, so velocity data below this boundary corresponding to the crystalline rock is unavailable, as diffraction energy is not observed traveling through it.

In general the deterministic and equal weight diffraction images contain more background noise than the probabilistic image, although all three methods are able to isolate weak diffractions in the décollement at about 7.2 s and identify the lowest sedimentary region between the décollement and crystalline rock transition at 7.5 s as relatively free of diffraction energy.

Examining the gathers centered at 4100 m, notice that much of the energy present in the complete image slope gather, Figure 19a, surrounds the dominant slope denoted by the dashed fuchsia line. This is expected, as reflection signal is often the most powerful feature of a seismic image. The stationary reflection energy surrounding that line is not present in the other gathers, as it has been mostly removed by plane wave destruction – notice in the deterministic gather, Figure 19b, that energy around the dominant slope is significantly suppressed. Although not a central argument in this paper, this is interesting because it illustrates how the deterministic diffraction imaging workflow employed in the creation of this image, which was based on reflection removal by removing energy possessing the dominant slope in the data domain as identified by plane-wave destruction filters following Fomel (2002), has a similarity to the diffraction imaging method of Moser and Howard (2008), which involves directly applying a mute around the dominant slope in gathers similar to these to surpress stationary reflection energy. In effect, the plane-wave destruction process has generated similarly muted data when viewed in these gathers. A key difference, is that plane-wave destruction is able to at least partially differentiate between diffraction energy underlying reflection energy rather than completely masking it. This feature is particularly apparent in the two gathers when dominant slopes are near zero, as can be seen near 6.1 s and 7.4 s where energy remains near the dominant slope value in the deterministic gather.

The three diffraction image gathers, the deterministic gather of Figure 19b, the equal weight gather of Figure 19c, and the probabilistic gather of Figure 19d, have significantly different appearance. Although energy near the complete image gather's dominant slope tends to be suppressed in all three gathers, as one would expect from diffraction images, the ranges over which energy is present differs significantly. Most energy in the equal weight gather is confined within ± 0.003 s^2/m, while that of the other two gathers has a larger range, with at least some energy extending the width

of each gather. The probabilistic weight gather has a more sparse, coherent, and clean appearance when compared to the other two, while the deterministic gather features more chaotic, less coherent features. The deterministic gather also features some interesting coherent energy isolated to slope values with magnitudes greater than 0.005 s^2/m which is likely tied to out of plane diffractions, reflection energy that does not have the dominant slope at a location, or migration artifacts. An example of such an feature occurs in the deterministic gather between 6.2 and 6.4 s, which corresponds to events in the deterministic diffraction image, Figure 18b, sloping steeply downward to the right at 4100 m between 6.2 and 6.4 s. In this case they appear to be related to reflections off of a dipping fault interface cutting through the strata which define dominant slope. Although these features are interesting and can be useful for identifying faults, they are not diffractions. Also notice that within the three diffraction gathers, coherent energy is not present between 6.5 and 6.7 s. Indeed, in the probabilistic gather very little energy at all is present in that interval, and thus the probabilistic diffraction image, Figure 18d is mostly blank in that interval at 4100 m. However, in both the deterministic diffraction image, Figure 18b, and the equal weight diffraction image, Figure 18c, that area contains noisy, chaotic energy, which based on its appearance in the corresponding gathers is not related to diffraction.

A final noteworthy feature is visible between 6.7 and 6.85 in three gathers. Here we see a polarity reversal in flat flat diffraction energy for slope values near 0.001 s^2/m. This polarity reversal is an excellent example of diffractions caused by an edge rather than a point (Klem-Musatov et al., 2008). In this case, the diffraction is likely caused by a fault fault which has created a material discontinuity. This illustrates a situation where the assumption that diffractions are laterally coherent across all slopes, which is valid for point diffractions and justifies the use of gather semblance as a measure of diffraction, may not hold. Fortunately, in this case these edge diffractions are successfully resolved by the probabilistic process, the corresponding event can be seen at 4100 m beginning around 6.7 s in Figure 18d.

The probabilistic diffraction imaging process outputs a plausible RMS expectation velocity, Figure 17a using velocity analysis on data already stacked to zero offset. Because the calculated velocity field is relatively stable, we are able to calculate Dix velocity and transform our images from time to the depth domain in the manner of Sripanich and Fomel (2018).

Figures 20b and 20a contain the probabilistic diffraction image of Figure 18d and complete image of Figure 20a transformed to the depth domain and plotted with a true aspect ratio relating their horizontal and vertical components. Features, including the décollement near 5.6 km depth, the crystalline rock transition near 6 km depth, the seafloor, and thrust faults are visible in the diffraction and complete images. Reflections corresponding to highly deformed strata in an accretionary prism undergoing shortening and thickening and extending from the décollement to the seafloor are visible in the reflection image. In this image, the overriding Eurasian plate has relative motion to the left, towards the Philippine Sea and the subducting

Philippine Plate has relative motion to the right, towards the Japanese island of Honshū.

We calculate Dix, or interval, velocity using the RMS velocity field, and transform it to the depth domain. Depth domain Dix velocity is overlaid by the depth stretched complete image, and shown in Figure 20c to provide context for the velocity field. Velocities calculated in the probabilistic imaging process are reasonable when compared to seismic velocity measurements in the region performed by the Integrated Ocean Drilling Program using core data and bore holes in the area (Moore et al., 2009). Examining the Dix velocity, we see a general trend of increasing velocity with depth until the area of the décollement near 5.7 km depth, were velocity begins decreasing. Additionally, areas where the décollement is intersected by faults tend to have higher Dix velocities than surrounding areas. This is related to the fact that thrust faults extending from the décollement to the seafloor act as conduits facilitating the dewatering and compaction of sediments overlaying the décollement. The thrust faults do not extend below the décollement, so water has more difficulty escaping, hindering compaction and leading to lower velocities as well as a low velocity anomaly below the feature. This anomalous low corresponds to the deepest reliable velocity information from this study. Because we do not observe diffractions below the layer of strong diffractions at approximately 6 km marking the transition to crystalline rock, our study does not provide information about the presumably higher velocities underlying that transition.

CONCLUSIONS

We formulate and apply a probabilistic approach to seismic diffraction imaging. By treating the weight functions in path-integral imaging as diffraction likelihood, we are able to emphasize wavefield components in seismic images output by OVC that are the most likely to correspond to a properly migrated seismic diffraction image and suppress the wavefield components that are not likely diffractions, improving the signal to noise ratio. The toy model example illustrated how the probabilistic imaging process attenuated reflection energy and amplifies diffraction energy without explicit separation of the two, but rather as a result of applying weights to partial images. Thus, the method may be used in tandem with data-domain diffraction separation techniques to suppress any remnant reflection energy, as was done in the Nankai trough field data example. The process may attenuate some high frequency diffraction information, making it better suited for imaging diffractions in noisy environments. The synthetic experiment in this paper illustrated how the probabilistic method can be robust in such environments, creating an image featuring strong diffractions and suppressing noise with a RMS value 16 times greater than that of the noiseless diffraction energy. That synthetic experiment also demonstrated how the method has greater success imaging strong diffractions than weak ones and may have difficulty imaging diffractions whose moveout tails are superimposed by the tails of stronger overlaying diffractions. Diffractions imaged by the probabilistic process are laterally coherent in

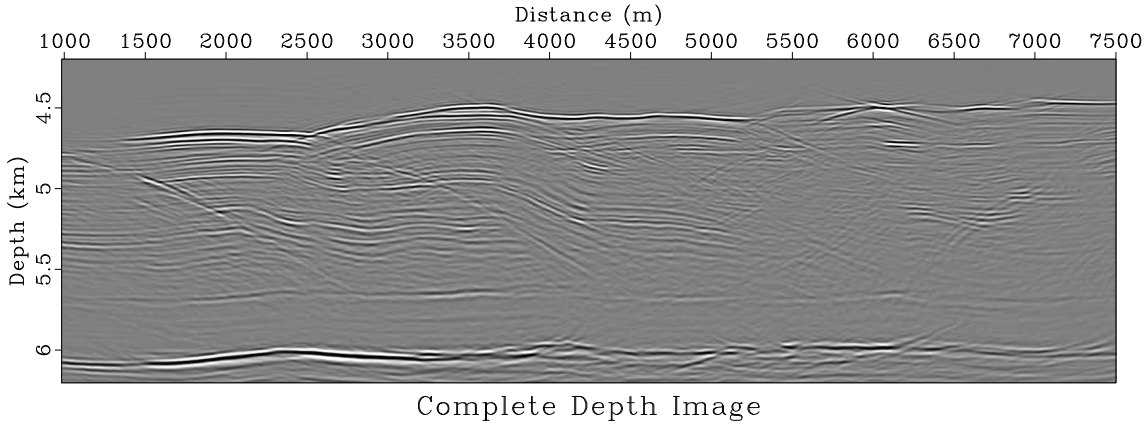

(a)

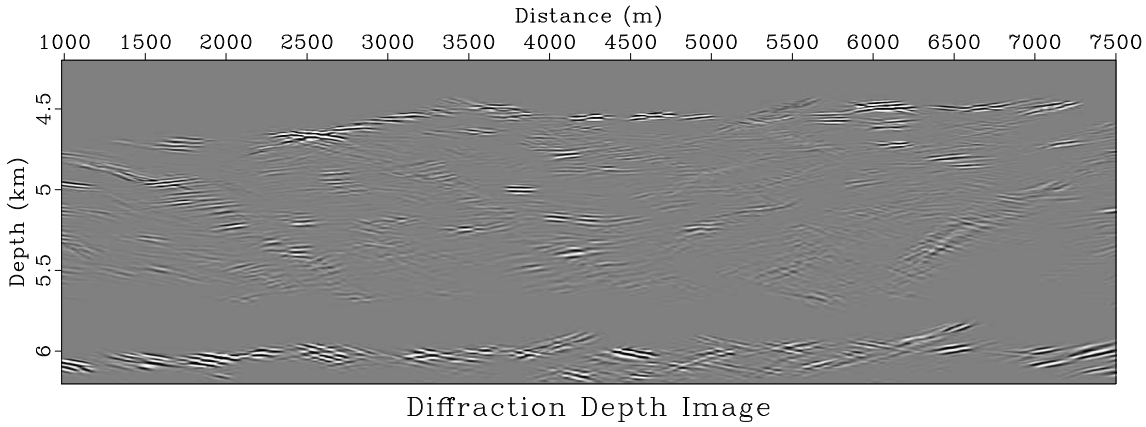

(b)

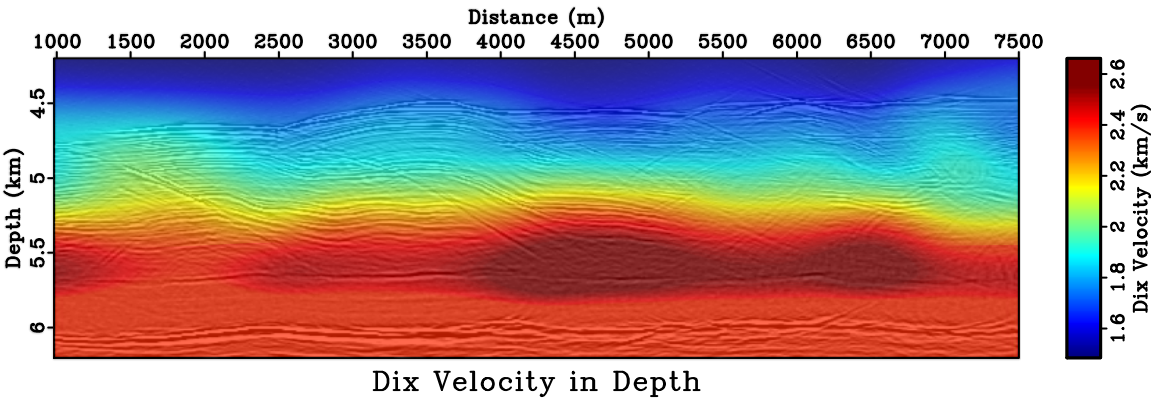

(c)

Figure 20: Nankai Trough images and velocities transformed from the time to depth domains: (a) complete image; (b) probabilistic diffraction image; (c) Dix velocity overlaid with complete image.

slope gathers because the weights are built from gather semblance. Correctly imaged diffraction energy is typically laterally coherent, but this assumption may be violated when energy from other diffractions becomes superimposed on a the slope gather centered above a correctly migrated diffraction. Therefore, this method should not be thought of as seeking to image every single diffractor within a seismic volume, or being superior to deterministic diffraction imaging, but rather as a supplementary tool to conventional diffraction imaging methods, outputting a image that identifies features that we can say with some certainty are correctly migrated diffractions. This can aid in the process of identifying geologically interesting features like the seafloor, faults, décollement or the transition from sedimentary to crystalline rock, seen in the field data example from the Nankai trough.

Creating a probabilistic diffraction image through the proposed process does not require a migration velocity as an input, but rather generates one as an output. This means that direct comparison of the diffractions resolved by the deterministic image and the probabilistic image in the noiseless synthetic experiment as a measure of the probabilistic method's utility is not particularly meaningful, as that deterministic image in a noiseless environment with perfect apriori information of the subsurface velocity is effectively the best diffraction image one could hope to achieve in a single migration (although least-squares or sparse inversion techniques could yield a better resolved diffraction image iteratively (Merzlikin et al., 2020)). Instead, the probabilistic imaging method determines the most likely velocity field, as well as a measure of velocity uncertainty, as it operates. That output migration velocity may also be determined using a single offset of data, as was the case in the experiments presented in this paper. The expectation velocity produced in the synthetic experiments presented here tracked the correct migration velocity to within one standard deviation, and for the Nankai Trough field data example output reasonable velocities that resolved a velocity inversion. The process of finding the expectation velocity requires diffraction information, so the method's ability to determine correct migration velocities may be limited where diffractions are not present, as seen in the toy model example and in the Nankai Trough example below the transition to crystalline rock.

The challenges encountered in the studies featured in this paper introduce some promising directions for future inquiry. The difficulties faced by the probabilistic method at resolving a large dynamic range of diffractions could be mitigated by decreasing the dynamic range of the weight functions by using, for example, powers of the combined weights, although that would also make the method more susceptible to noise. Finding the powers of weight functions that best balance highlighting diffraction signal and noise could improve the method. Similarly, finding more sophisticated ways of normalizing the weights to preserve weak diffraction and exploring other weights tied to the likelihood of diffraction could yield improved results. Particularly interesting is exploring different measures of diffraction "flatness," or diffraction likelihood, than semblance in the slope-gather domain. Such measures may not be ideal in the presence of edge diffractions, as seen in the field data example. Although the probabilistic imaging process using semblance was able to resolve those edge diffractions, a better method may exist. Applying the weighted imaging process to

3D Oriented Velocity Continuation should also enhance the output diffraction images, as that would be able to account for the possible effects of out of plane diffractions and reduce the effect of intersecting diffraction tails on semblance. The concept of probabilistic weighting for path-integral imaging can be used for collections of images where the wavefront is parameterized by more variables than just migration velocity, making application to sets images output by other time migration parameters with a continuation operators a fascinating direction of inquiry. As an anisotropic continuation operator already exists, pursuing a similar framework to determine weights based on both velocity and anisotropy, as well as using the method to determine conditional probability for anisotropy for each migration velocity, seems promising.

The ability of the method to suppress noise, highlighted in the noisy synthetic experiment, suggests that applying this method to passive seismic data could be beneficial and makes it a promising direction of future inquiry. Geophone station signals could be used as input data for the continuation process with an extra event time, t_o variable added. This variable would correspond to earthquake event time in the seismic record. This extra variable could be applied as a shift on t prior to performing OVC and the probabilistic imaging process. Weights could be treated as conditional probabilities given event time t_o. Parallelization in t_o would be a relatively straightforward process, making the expensive required computations feasible.

Probabilistic path-integral diffraction imaging does not require advance knowledge of the migration velocity, which it generates as an output. Additional weights may be used to improve the results, and the method could be modified to emphasize different portions of the wavefield. Theoretically, this approach should function for not just velocity, but any time migration parameter with a continuation operator, so application to anisotropic imaging is a promising direction for future work.

ACKNOWLEDGEMENTS

We are grateful to Texas Consortium for Computational Seismology sponsors for financial support of this research, Nathan Bangs for discussions about the Nankai Trough's geology, Tan Bui and Dmitrii Merzlikin for inspiring conversations, and developers of and contributors to the Madagascar open source software project (Fomel et al., 2013).

REFERENCES

Bangs, N. L. B., G. F. Moore, S. P. S. Gulick, E. M. Pangborn, H. J. Tobin, S. Kuramoto, and A. Taira, 2009, Broad, weak regions of the Nankai Megathrust and implications for shallow coseismic slip: Earth and Planetary Science Letters, **284**, no. 1, 44–49.

Berkovitch, A., I. Belfer, Y. Hassin, and E. Landa, 2009, Diffraction imaging by multifocusing: Geophysics, **74**, no. 6, WCA75–WCA81.

Burnett, W., and S. Fomel, 2011, Azimuthally anisotropic 3D velocity continuation: International Journal of Geophysics, **2011**, Article ID 484653.

Burnett, W., S. Fomel, and R. Bansal, 2011, Diffraction velocity analysis by path-integral seismic imaging: 81st Annual International Meeting, SEG, Expanded Abstracts, 3898–3902.

de Figueiredo, J. J. S., F. Oliveira, E. Esmi, L. Freitas, J. Schleicher, A. Novais, P. Sussner, and S. Green, 2013, Automatic detection and imaging of diffraction points using pattern recognition: Geophysical Prospecting, **61**, 368–379.

Decker, L., and S. Fomel, 2014, Diffraction imaging and velocity analysis using oriented velocity continuation: 84th Annual International Meeting, SEG, Expanded Abstracts, 4810–4815.

Decker, L., X. Janson, and S. Fomel, 2015, Carbonate reservoir characterization using seismic diffraction imaging: Interpretation, **3**, no. 1, SF21–SF30.

Decker, L., and A. Klokov, 2014, Diffraction extraction by plane-wave destruction of partial images: 84th Annual International Meeting, SEG, Expanded Abstracts, 3862–3867.

Decker, L., A. Klokov, and S. Fomel, 2013, Comparison of seismic diffraction imaging techniques: plane wave destruction versus apex destruction: 83rd Annual International Meeting, SEG, Expanded Abstracts, 4054–4059.

Decker, L., D. Merzlikin, and S. Fomel, 2017a, Diffraction imaging and time-migration velocity analysis using oriented velocity continuation: Geophysics, **82**, no. 2, U25–U35.

———, 2017b, Enhancing seismic-diffraction images using semblance-weighted least-squares migration: 87th Annual International Meeting, SEG, Expanded Abstracts, 5294–5299.

Fomel, S., 2002, Applications of plane wave destruction filters: Geophysics, **67**, no. 6, 1946–1960.

———, 2007, Local seismic attributes: Geophysics, **72**, no. 3, A29–A33.

Fomel, S., E. Landa, and M. T. Taner, 2007, Poststack velocity analysis by separation and imaging of seismic diffractions: Geophysics, **72**, no. 6, U89–U94.

Fomel, S., P. Sava, I. Vlad, Y. Liu, and V. Bashkardin, 2013, Madagascar: open-source software project for multidimensional data analysis and reproducible computational experiments: Journal of Open Research Software, **1**, no. 1, e8.

Fomel, S. B., and E. Landa, 2014, Structural uncertainty of time-migrated seismic images: Journal of Applied Geophysics, **101**, 27–30.

Forel, D., T. Benz, and W. D. Pennington, 2005, Seismic Data Processing with Seismic Un*x: A 2D Seismic Data Processing Primer: Society of Exploration Geophysicists.

Harlan, W., J. Claerbout, and F. Rocca, 1984, Signal to noise separation and velocity estimation: Geophysics, **49**, no. 11, 1869–1880.

Kaur, H., S. Fomel, and N. Pham, 2019, Elastic wave-mode separation in heterogeneous anisotropic media using deep learning, *in* SEG Technical Program Expanded Abstracts 2019: Society of Exploration Geophysicists, 2654–2658.

Khaidukov, V., E. Landa, and T. Moser, 2004, Diffraction imaging by focusing-defocusing: an outlook on seismic super resolution: Geophysics, **56**, 1478–1490.

Klem-Musatov, K., 1994, Theory of seismic diffractions: Society of Exploration Geophysicists.

Klem-Musatov, K., A. M. Aizenberg, J. Pajchel, and H. B. Helle, 2008, Edge and Tip Diffractions: Theory and Applications in Seismic Prospecting: Society of Exploration Geophysicists.

Klokov, A., and S. Fomel, 2012, Separation and imaging of seismic diffractions using migrated dip-angle gathers: Geophysics, **77**, no. 6, S131–S143.

———, 2013, Selecting an optimal aperture in Kirchhoff migration using dip-angle gathers: Geophysics, **76**, no. 6, S243–S254.

Kozlov, E., N. Baransky, E. Korolev, A. Antonenko, and E. Koshchuck, 2004, Imaging scattering objects masked by specular reflections: 74th Annual International Meeting, SEG, Expanded Abstracts, 1131–1134.

Landa, E., 2012, Seismic diffraction: wheres the value?: 82nd Annual International Meeting, SEG, Expanded Abstracts, 1–4.

Landa, E., S. Fomel, and T. Moser, 2006, Path-integral seismic imaging: Geophysical Prospecting, **54**, 491–503.

Landa, E., S. Fomel, and M. Reshef, 2008, Separation, imaging, and velocity analysis of seismic diffractions using migrated dip-angle gathers: 78th Annual International Meeting, SEG, Expanded Abstracts, **27**, no. 1, 2176–2180.

Merzlikin, D., and S. Fomel, 2017, Analytical path-summation imaging of seismic diffractions: Geophysics, **82**, no. 1, S51–S59.

Merzlikin, D., S. Fomel, and M. K. Sen, 2019, Least-squares path-summation diffraction imaging using sparsity constraints: Geophysics, **84**, S187–S200.

Merzlikin, D., S. Fomel, and X. Wu, 2020, Least-squares diffraction imaging using shaping regularization by anisotropic smoothing: Geophysics, **85**, S313–S325.

Moore, G., and T. Shipley, 1993, Character of the décollement in the Leg 131 area, Nankai Trough: ed Hill, IA, Proc. scientific results, ODP, Leg 131, Nankai Trough, 73–82.

Moore, G. F., N. L. Bangs, A. Taira, S. Kuramoto, E. Pangborn, and H. J. Tobin, 2007, Three-Dimensional Splay Fault Geometry and Implications for Tsunami Generation: Science, **318**, no. 5853, 1128–1131.

Moore, G. F., J. O. Park, N. L. Bangs, S. P. Gulick, H. J. Tobin, Y. Nakamura, S. Sato, T. Tsuji, T. Yoro, H. Tanaka, S. Urakai, Y. Kido, Y. Sanada, S. Kuramoto, A. Taira, and the Expedition 314/315/316 Scientists, 2009, Structural and seismic stratigraphic framework of the NanTroSEIZE Stage 1 transect: Proceedings of the Integrated Ocean Drilling Program, 1–46.

Moore, G. F., T. Shipley, P. Stoffa, D. Karig, A. Taira, S. Kuramoto, H. Tokuyama, and K. Suyehiro, 1990, Structure of the Nankai Trough accretionary zone from

multichannel seismic reflection data: Journal of Geophysical Research: Solid Earth, **95**, no. B6, 8753–8765.

Moser, T., and C. Howard, 2008, Diffraction imaging in depth: Geophysical Prospecting, **56**, 627–641.

Nemeth, T., C. Wu, and G. T. Schuster, 1999, Least-squares migration of incomplete reflection data: Geophysics, **64**, no. 1, 208–221.

Pham, N., S. Fomel, and D. Dunlap, 2019, Automatic channel detection using deep learning: Interpretation, **7**, SE43–SE50.

Popovici, A. M., I. Sturzu, and T. J. Moser, 2015, High resolution diffraction imaging of small scale fractures in shale and carbonate reservoirs: 14th International Congress of the Brazilian Geophysical Society, H1–2–6.

Reshef, M., and E. Landa, 2009, Post-stack velocity analysis in the dip-angle domain using diffractions: Geophysical Prospecting, **57**, no. 5, 811–821.

Schleicher, J., and J. C. Costa, 2009, Migration velocity analysis by double path-integral migration: Geophysics, **74**, no. 6, WCA225–WCA231.

Schwarz, B., 2019, Chapter one - an introduction to seismic diffraction, *in* Recent Advances in Seismology: Elsevier, volume **60** *of* Advances in Geophysics, 1–64.

Sripanich, Y., and S. Fomel, 2018, Fast time-to-depth conversion and interval velocity estimation in the case of weak lateral variations: Geophysics, **83**, no. 3, S227–S235.

Tschannen, V., N. Ettrich, M. Delescluse, and J. Keuper, 2020, Detection of point scatterers using diffraction imaging and deep learning: Geophysical Prospecting, **68**, 830–844.

Wu, X., Z. Geng, Y. Shi, N. Pham, S. Fomel, and G. Caumon, 2020, Building realistic structure models to train convolutional neural networks for seismic structural interpretation: Geophysics, **85**, WA27–WA39.